An Energy-Efficient and Bandwidth-Scalable DWDM Heterogeneous Silicon Photonics Integration Platform

Di Liang, *Senior Member, IEEE*, Sudharsanan Srinivasan, *Member, IEEE*, Geza Kurczveil, *Member, IEEE*, Bassem Tossoun, Stanley Cheung, *Member, IEEE*, Yuan Yuan, Antoine Descos, Yingtao Hu, Zhihong Huang, Peng Sun, *Member, IEEE*, Thomas Van Vaerenbergh, Chong Zhang, Xiaoge Zeng, Songtao Liu, John E. Bowers, *Life Fellow, IEEE*, Marco Fiorentino, and Raymond G. Beausoleil, *Senior Member, IEEE*

(Invited Paper)

***Abstract*—Heterogeneous III-V-on-silicon photonic integration has proved to be an attractive and volume manufacturable solution that marries the merits of III-V compounds and silicon technology for various photonic integrated circuit (PIC) applications. The current main-stream Ethernet trends for larger bandwidth are pushing higher modulation baudrate or employing advanced modulation format for datacom applications. However, neither solution is likely able to significantly drive overall solution cost and energy efficiency to the best sweet spot, nor to unfold the full potential of heterogeneous integration. Here we review our innovations on a special heterogeneous III-V-on-silicon platform, and the development of a dense wavelength division multiplexed (DWDM) transceiver. A 40-channel DWDM architecture and platform fabrication are discussed first, followed by experimental demonstration of each high-quality building block. InAs/GaAs quantum dot material is the choice for building robust multi-wavelength lasers, amplifiers, and high-speed avalanche photodetectors (APDs) which complements the more mature SiGe APDs. A metal-oxide-semiconductor capacitor phase shifter is a mission critical structure to provide athermal and efficient tuning for deinterleavers and microring resonators, and high-speed modulation. A successful 8 × 25 Gb/s link demonstration paves the way for the world's first fully-integrated DWDM PIC on Si with Terabit/s aggregated bandwidth and energy efficiency likely to ∼100 fJ/bit.**

***Index Terms*—Silicon photonics, wavelength division multiplexing, heterogeneous integration, quantum dot lasers.**

Manuscript received January 14, 2022; revised March 30, 2022; accepted March 31, 2022. Date of publication June 13, 2022; date of current version June 29, 2022. This work was supported by ARPA-E OPEN Program under Grant DE-AR0001039. *(Corresponding author: Di Liang.)*

Di Liang, Sudharsanan Srinivasan, Geza Kurczveil, Bassem Tossoun, Stanley Cheung, Yuan Yuan, Antoine Descos, Yingtao Hu, Zhihong Huang, Peng Sun, Thomas Van Vaerenbergh, Chong Zhang, Xiaoge Zeng, Marco Fiorentino, and Raymond G. Beausoleil are with the Hewlett Packard Labs, Milpitas, CA 95035 USA (e-mail: di.liang@ieee.org; sudharsanan@ee.iitm.ac.in; geza.kurczveil@hpe.com; bassem.tossoun@hpe.com; stanley.cheung@hpe.com; yuan.yuan@hpe.com; antoine.descos@hpe.com; yingtao.hu@hpe.com; zhihong.huang@hpe.com; psun@hpe.com; thomas.van-vaerengbergh@hpe.com; chong.zhang@hpe.com; xiaoge.zeng@hpe.com; marco.fiorentino@hpe.com; ray.beausoleil@hpe.com).

Songtao Liu and John E. Bowers are with the Department of Electrical and Computer Engineering, University of California, Santa Barbara, CA 93106 USA (e-mail: stliu@ece.ucsb.edu; bowers@ece.ucsb.edu).

Color versions of one or more figures in this article are available at https://doi.org/10.1109/JSTQE.2022.3181939.

Digital Object Identifier 10.1109/JSTQE.2022.3181939

I. Introduction

As A distinctive technology in fiber-optic communication, wavelength division multiplexing (WDM), along with the invention of Erbium-doped optical fiber amplifiers, led to the revolutionary transformation of long-haul communications to the fourth generation whichdoubles the transmission capacity over the previous generation of 30 years ago. Transmission of multi-channel signal through different wavelength carriers within existing single-mode fibers significantly reduces the infrastructure investment in new fiber deployment. It pushes back widely commercial adoption of coherent technology by at least one generation. Nowadays, dense wavelength division multiplexing (DWDM) with 50 or 100 GHz channel spacing in the C-band, combined with coherent technology, bears the burden of global transcontinental and metro data traffic.

Today, zettabytes of data are generated and nearly doubled every two years, and 80% of them are being transmitted within data centers. But limited input/output (I/O) solutions, i.e., high-end copper links (<10 m) and the 1st-generation vertical-cavity surface-emitting lasers (VCSELs)-based multi-mode active optical cables (AOCs) (<100 m), are quickly losing their viable dominance territories.On one hand, the demand for shorter reach bandwidth between servers and switches in data centers or among computing nodes in supercomputers is increasing. On the other hand, the scale of data center infrastructure is rapidly expanding, such as the 10.7 million square feet of space in the world's largest data center owned by China Telecom in Hohhot, Inner Mongolia, China [1]. While planar single-mode transceiver (TRx) chips and single-mode fiber easily extend the reach to 2 and then 10 km, uncooled operation requirements have led to the Ethernet standard specification based on parallel single-mode 4 lane (PSM4) or coarse wavelength division multiplexing of 4 wavelengths (CWDM4) with 20 nm grid in the O-band. Higher baudrate (>56 Gbaud/s) and pulse amplitude modulation 4-level (PAM4) are present mainstream bandwidth expansion solutions for post-100 G pluggable products. 4 × 100 Gb/s/lane PAM4 have became the primary format of 400 G products. Both directly and externally modulated transmitters

This work is licensed under a Creative Commons Attribution 4.0 License. For more information, see https://creativecommons.org/licenses/by/4.0/

with $>$100 Gb/s non-return-to-zero (NRZ) on–off keying (OOK) format or $>$200 Gb/s PAM4 or even PAM8 format have also been demonstrated [2]–[7]. As the datacom market continues to embrace PAM-based modulation formats and the CWDM4 or potentially CWDM8 standards, the community is also considering coherent technology to handle much larger intra-data center traffic of future generations. Such Ethernet-based roadmap ahead appears to deviate from some motivations and aspirational goals to use fiber-optic interconnects and develop a new dense photonic integration platform on silicon (Si) in the first place, i.e., high energy efficiency and low total cost of ownership, i.e., "CapEx+OpEx". Both ultra-high baudrate and advanced modulations like PAMx and then coherent communications gain bandwidth at the expense of a) much higher demand on light source output power and linewidth; b) increasingly heavy dependence on power-hungry digital signal processing (DSP), c) increased latency and reducing reliability in datacom harsh environment. They translate into more power consumption in photonic and electronic chips and overall datacenter thermal management (OpEx), and higher cost on TRx hardware (CapEx). On the other hand, high performance computing (HPC), conventionally referring to supercomputers, is emerging as new high-end functionality and demanding service in data centers for artificial intelligence and machine learning applications. Apparently, the aforementioned mainstream Ethernet progressing trend points to an opposite direction to meet the top three technical priorities in HPC interconnect, i.e., latency (aiming sub-μs in Exascale machines), bandwidth and power consumption, plus pressure to stall rising hardware cost proportion on total HPC network.

Other than ultra-high baudrate and advanced modulation, parallelization is another mature option to increase the aggregated bandwidth while other multiplexing approaches are still in research stage. The solution for more parallel lanes will ultimately be limited by the physical dimension of the package due to finite spacing of the cores in fiber ribbon, in addition to investing in laying more or new type of fibers. Multi-core fibers bring incremental increase in the number of channels, but face new challenges in optical coupling, limited reach and higher cost. Therefore, DWDM has been a long-term vision for optical interconnect R&D in Hewlett Packard Labs (HPL) [8], [9]. The gain from increased channel count (i.e., higher spectral efficiency) by a factor of 170+, assuming 60 GHz DWDM channel spacing in a minimal CWDM4 window of 60 nm in the O-band, results in a theoretical aggregated data rate of $\geq$2.7$-$4.25 Tb/s/fiber when using a medium OOK modulation at 16-25 Gb/s. A design to utilize 16 or 32 wavelengths per link for more simplified multi-wavelength laser source enablement and system control is also a compelling solution providing up to 800 Gb/s/fiber bandwidth at 25 Gb/s/λ. As long as channel crosstalk can be well suppressed, an error-free transmission with bit error rate (BER) of 10^{-12} has been demonstrated [10], eliminating excess delay and power consumption from error correction. Previous study on DWDM links including all major power-consuming optical and electronic elements concluded that the energy efficiency sweet spot was around 8 Gb/s/λ [11]. While a similar study is required to reflect new benchmarks in CMOS drivers, each new element in the TRx link, and recent innovations in architecture and energy-efficient control, we don't foresee the energy sweet spot to drift beyond 40 Gb/s/λ. The new technical challenges will apparently come from complex system design and intelligent channel coordination in temperature-fluctuating datacom environments without luxury of precise grid management in long-haul DWDM system. DWDM has also traditionally been considered a more expensive solution than CWDM due to its higher design complexity, larger device count and more precise control requirement. Therefore, large-scale photonic integration becomes a logic solution to adopt. From the perspectives of integration and bandwidth density, link loss budget, device innovation, chip size, and eventually low-cost volume production, Si photonics is a preferable platform over conventional solutions of discrete component assembly or pure III–V photonic integration.

In this paper, we welcome and appreciate the opportunity to review our recent progress towards demonstration of the world's first fully-integrated DWDM platform on Si and TRx system implementation strategies. First, the DWDM TRx architecture and integration platform are introduced. A detailed review of key building block design and performance in different stages of on-going research is provided. Perspectives on meeting device coordination, channel control, and system power consumption requirements are discussed to project performance benchmarks for such a fully-integrated DWDM TRx in the near future.

II. DWDM Transceiver Architecture

HPL's first generation (Gen-1) DWDM TRx design relies on a stand-alone III–V O-band InAs/GaAs quantum-dot (QD) comb laser as a multi-wavelength source to power a fully CMOS-compatible, single-bus and microring resonator-based TRx on Si-on-insulator (SOI) substrate [8], [12]. A 24-ch. Si photonics DWDM TRx made by a leading CMOS foundry and 3D packaged with CMOS driver chip and fiber ribbon was demonstrated very recently [13]. A high energy efficiency of 1 pJ/bit was just measured on the Rx part while Tx testing is on-going [13]. In parallel, the second generation (Gen-2) DWDM TRx architecture shown in Fig. 1 was also proposed and being developed [14]–[16]. A similar modelocked comb laser either heterogeneously [17]–[19] or monolithically [19]–[23] integrated on Si generates tens or hundreds of evenly-spaced wavelengths within a reasonable power variation, e.g., 3 dB [24]. This leads to significant reduction in the number of required wavelength-stabilized continuous-wave (cw) lasers, e.g., distributed feedback (DFB) or distributed Bragg reflector (DBR) lasers. The comb lasers are comparable in size to typical DFB and DBR lasers, and their spectral channel spacing is a function of the photolithography-defined laser cavity. These factors tremendously simplify fabrication, channel spacing control, footprint and cost. Quantum dot (QD) instead of quantum well (QW) gain medium is believed to be more capable of enabling high-quality comb lines due to QD's intrinsic material properties [17], [25], [26]. Optional QD semiconductor optical amplifier(s) (SOAs) can be readily integrated to boost up the comb line intensity either immediately after the comb laser or after data modulation as shown in Fig. 1 or even in the receiver end as pre-amplifier(s). Up to 39 dB on-chip gain with 23 dBm

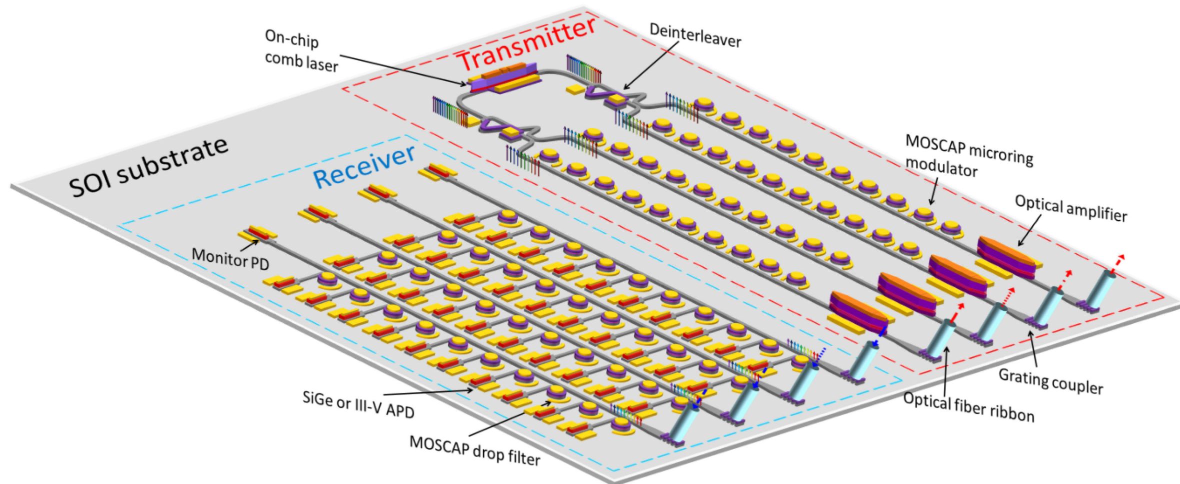

Fig. 1. Schematic of a fully-integrated 40-ch. DWDM TRx on a heterogeneous III–V-on-Si platform.

saturation power have been reported on a 5 mm-long monolithic QD SOA on Si [27]. More details will be discussed in the Section IV later.

Depending on the power and wavelength spacing from the comb source, the modulation rate per channel, the nonlinearity threshold in the microring resonators, and link loss budget, one multi-wavelength comb stream can be split into two or more streams through either optical power splitter(s) or wavelength deinterleaver(s) or a combination of both [14]. Such spatial division multiplexing (SDM) design offers advantages of bandwidth scaling or/and good signal integrity in this DWDM-SDM link. Each power splitting doubles channel count and aggregated bandwidth subsequently. One slight advantage in heterogeneous on-chip comb laser vs. off-chip comb source configuration is convenience to realize a symmetric dual output configuration to eliminate an on-chip power splitter if necessary. The effective wavelength spacing extension through the deinterleaver alleviates the challenge from tradeoff between gain length-determined comb laser efficiency (output power) vs. wavelength spacing, especially for monolithic comb lasers that do not operate in higher order harmonics. It also allows higher Nyquist frequency of OOK external modulation without suffering channel cross-talk quickly [28]. Both options offer another layer of system power and cost reduction, as the light source is known to be the most power-hungry and expensive single component in a photonic link, aside from the electronics.

Upon splitting into four parallel multi-wavelength streams as shown in Fig. 1, each stream is then fed into a compact microring modulator array for external OOK modulation at 25 Gb/s/ch. 100–120 GHz wavelength spacing is a design choice based on comb laser performance and minimal channel cross-talk [28], [29]. Each microring modulator bank consists of 10 microring modulators for an aggregated data rate of 1 Tb/s (4 $\times$ 10 $\times$ 25 Gb/s/ch.). Popular choices like Mach-Zehnder interferometer (MZI) modulators or electro-absorption modulators both requiring large/bulky (de)multiplexers ((DE)MUX) in a WDM system is not a viable choice here. They rapidly build up link loss budget, chip size and power consumption as channel count increases. As one of the favorite optical components in the academic research community, microring resonators, particuarly III–V and Si ones, are very spectrally sensitive to fabrication imperfections and environmental changes. They have long been regarded impractical by mainstream industrial applications where robust operation is a must. But its advantages, for instance, resonance enhancement, natural WDM characteristic, low insertion loss (IL), compactness, etc. translate to energy-efficient optical filtering and high-speed modulation with superior control agility [30]. We believe that their merits outweigh the inevitable system complexity which requires active tune and monitor the resonance positions for Tx-Rx coordination - a task that microelectronic circuits excel at. We note here that, unlike DFB or DBR lasers, the comb lasers are challenging to operate in absolute wavelength grids by design. Evenly-space wavelength stream drifts in the same pace as that of the Fabry-Perot (FP) lasers on the same material system when temperature fluctuates. This is another reason why comb lasers don't team up well with bulky components like array waveguide grating or Echelle grating and MZI modulators, where the agile and low-power phase tuning on those components with respect to the comb stream are impractical.

Thermo-optic tuning is the most widely used phase control method in Si photonics, and has been used in our Gen-1 DWDM Si photonics TRx. But it can easily consume 10–100 $\times$ more energy than actual Si microring-based modulation accordingly to our experiment. In this Gen$-$2 design, we employ a novel heterogeneous metal-oxide-semiconductor capacitor (MOSCAP) structure [31] to generate plasma dispersion effect for athermal and ultra-energy efficient phase tuning [32], not only in microring modulators [33], [34], but also in deinterleavers [35], DEMUX drop filters and soon in heterogeneous comb lasers as previously demonstrated in microring lasers [36].

Upon encoding the information into 40 MOSCAP microring modulators, the four parallel signal streams in TE polarization are boosted by respective heterogeneous QD SOAs if necessary, and reach a 1D TE-polarized grating coupler (GC) array for coupling with a single-mode fiber array. If polarization-maintaining

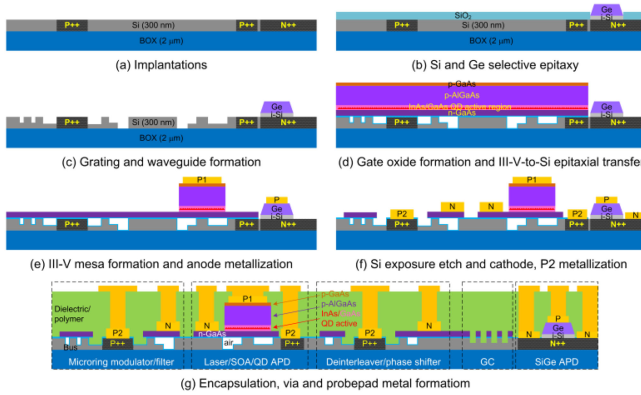

Fig. 2. Schematic fabrication flow of the major process steps.

(PM) fibers are used, four identical GCs serve as the receiver inputs on the same chip. Otherwise, 2D dual-polarization GCs [37] each followed by an optical power combiner are necessary but come with additional IL $\sim$3 dB. An optical isolator is likely required to be inserted in the fiber link to avoid feedback disturbing stable comb laser operation. Similar microring resonators, 10 in each bus waveguide, act as DEMUX to drop each channel's optical data into a corresponding highly sensitive photodetector (PD) to complete the receiver function. Two types of avalanche photodetectors (APDs) on Si [38], vizt., SiGe APDs and InAs/GaAs QD APDs, are being developed to detect weak optical signals for lowering source output power and subsequently total power consumption as much as possible. A target sensitivity of -20 dBm at 25 Gb/s for BER of 10^{-12} is set to achieve the sub-pJ/bit energy efficiency of this 1 Tb/s DWDM TRx. A brief discussion on link budget and system energy efficiency analysis will be conducted in Section V. Such a single TRx chip can be 3D integrated with only one CMOS driver chip and requires just one fiber ribbon attachment, reducing packaging complexity and cost as demonstrated in our Gen-1 TRx [13].

III. Platform Fabrication

Fig. 2 illustrates major processing steps of this heterogeneous Si photonics platform. Fabrication starts from multiple ion implantations on the SOI wafer to form p-type Si for MOSCAP microring modulators and heavily doped p++ and n++ regions for ohmic contacts of MOSCAP-based devices and SiGe APDs, respectively (Fig. 2(a)). Then selective epitaxial growth of thin intrinsic Si, lightly doped p-type Si and Ge with heavily doped p-type top surface can be conducted on top of the n++ region to form a SiGe APD mesa (Fig. 2(b)) similar to the one in [39]. Si epitaxy step or even metal contact on Ge can also be eliminated for different APD designs [40], [41]. The following step is to form passive photonic components and circuit, including gratings, deinterleavers, microring drop filters, waveguide and bonding-facilitating structures by a series of photolithography and dry etch cycles to different etch depth by design (Fig. 2(c)). Upon thorough clean on both patterned SOI wafer and blank InAs/GaAs QD samples, MOSCAP gate oxide is formed on both SOI and III–V wafer by deposition or oxidation, followed by selective molecule wafer bonding to placing QD samples in planar regions of the SOI wafer. Removal of the thick GaAs substrate and AlGaAs etch stop layer completes the III–V epitaxial transfer process with heavily doped p-GaAs on the top of this $\sim$2 μm thick QD laser stack (Fig. 2(d)). A photolithography and proton implantation is then used for electrical isolation between gain and saturable absorption (SA) sections in comb lasers, as well as for current channel formation for wide III–V mesa design. Once p-contact metal (terminal P1) is deposited on p-GaAs through a liftoff process for laser, SOAs and PDs, as well as on p-Ge for SiGe APDs, III–V mesa formation by dry etch to InAs/GaAs active region is conducted (Fig. 2(e)). A selective wet etch step is performed to expose n-GaAs contact layer, followed by lifting off the n-contact metal (terminal N) on it. The residual III–V material and gate oxide outside III–V-on-Si functional regions are then removed to expose Si surface for p-contact metal (terminal P2) on p++ Si. Cathodes can also be formed on SiGe APDs here (Fig. 2(f)). Upon this step, all active and MOSCAP-enabled components are realized. Then the wafer surface is encapsulated by thick dielectric or polymer after repaid thermal anneal to form ohmic contacts in all terminals. Finally vias through encapsulation layer are defined and probepad metal is lifted off to finish the fabrication. More details can be found in [26]. Fig. 2(g) shows cross-sectional schematic of all key building blocks. We note that all reviewed heterogeneous QD comb lasers, SOAs and QD APDs in this paper don't have the P2 MOSCAP control terminal yet. But a QD DFB MOSCAP laser with Fig. 2(e) cross sectional design has been demonstrated [42], and QD MOSCAP comb lasers are in the fabrication during this manuscript preparation. We also note that co-integration of SiGe and III–V on the same heterogeneous platform is still under development. So all heterogeneous components and SiGe ones reviewed in this work were fabricated separately. Eventually only one type of APDs will be used as high-speed detectors. In comparison to traditional heterogeneous InP-on-Si photonic integration, our InAs/GaAs QD-on-Si platform with integrated MOSCAP shares large similarity in process simplicity, but more design flexibility in system-on-chip photonic integration. InAs/GaAs QD material is more capable of covering a large spectral bandwidth and even providing decent photodetection functionality. A 4λ DFB laser array with 20 nm CWDM grid was recently demonstrated on a single QD gain medium [43]. There is no need to bond multiple III–V chips with different epitaxial designs, which keeps desirable process simplicity and yield as single-λ design but for multi-wavelength system-on-chip functionality. The MOSCAP structure is a result of simply one additional ion implantation and metallization on Si, but enables high-speed modulation and energy-efficient athermal phase control which can be naturally implemented in lasers [44], deinterleavers [35], microring modulators [33], DEMUX filtering for agile overall DWDM system control. Detailed discussion on platform key building blocks and material and device design merits are followed in the sections below.

IV. Key Building Block Development

A. Multiple-wavelength Sources

Both Si-based heterogeneous and monolithic comb lasers in this work are based on an InAs/GaAs QD gain structure grown by the Stranski-Krastanow growth mode in molecular-beam epitaxy (MBE) [45], which can be scaled up to 300 mm or more relatively easier than metal organic chemical vapor deposition (MOCVD). QD gain medium embraces several superior merits for light sources in general datacom applications and high-quality comb generation [25], [26], [46], [47]. Its nanometer-scale size and three dimensional energy barrier effectively reduces mode partition and relative intensity noises (RIN), and results in ultrafast gain recovery for quiet and stable (frequency or temporal) modelocked multi-wavelength operation. Larger optical gain bandwidth from QD's inhomogeneous broadening provides a foundation to enable a broad and flat comb for a large number of strongly lasing comb lines. High-temperature gain stability, especially for p-doped QDs, lower transparency current density and largely enhanced immunity to defects from epitaxy, device fabrication, packaging and operation are all beneficial to diode lasers and SOAs [48], [49]. In particular, defect immunity characteristic is a decisive advantage for recently rapid progress and record-performance of monolithic QD lasers on Si substrate [50], [51]. For nearly all heterogeneous devices composed of an III–V diode structure on Si, the active region is inevitably exposed, causing dangling bonds-induced non-radiative recombination. Smaller surface recombination velocity and diffusion length in QDs minimize its impact on device efficiency, dark current and reliability [47].

One primary drawback for QD lasers, however, is their limited output power due to small dot size and density ($\sim 10^{10}$ cm^{-2}) and subsequently small gain volume and quick gain saturation [52]. Multi-wavelength lasing certainly poses more challenges, so individual comb line intensity from typical QD comb lasers is hardly over 3 dBm, assuming a minimal 8 lines within 3 dB power variation. Long laser cavity/gain lengths in the order of a few millimeters usually provide sufficient gain. But it results in an ultra-small native channel spacing, i.e., repetition rate (e.g., <10 GHz), defined by the cavity free spectral range (FSR) in Eq. 1 below:

$$FSR = \frac{\lambda_0^2}{2n_g L} \tag{1}$$

where λ_0, n_g and L are wavelength in vacuum, group refractive index of the lasing mode, and laser cavity length, respectively. As discussed before, one-stage wavelength deinterleaving can double the channel spacing. But multi-stage design adds up footprint and IL as well. A widely used method to overcome this tradeoff is to force higher order harmonics by placing one or multiple SAs in the middle of the cavity to suppress every other or every few other modes [54], respectively. The penalty, however, is higher internal loss from more optical absorption. Another simpler solution unique to the heterogeneous platform here is to leverage low propagation loss in Si and small transition loss between heterogeneous mode and Si waveguide mode with an adiabatic taper, and build an external laser cavity [55]. As

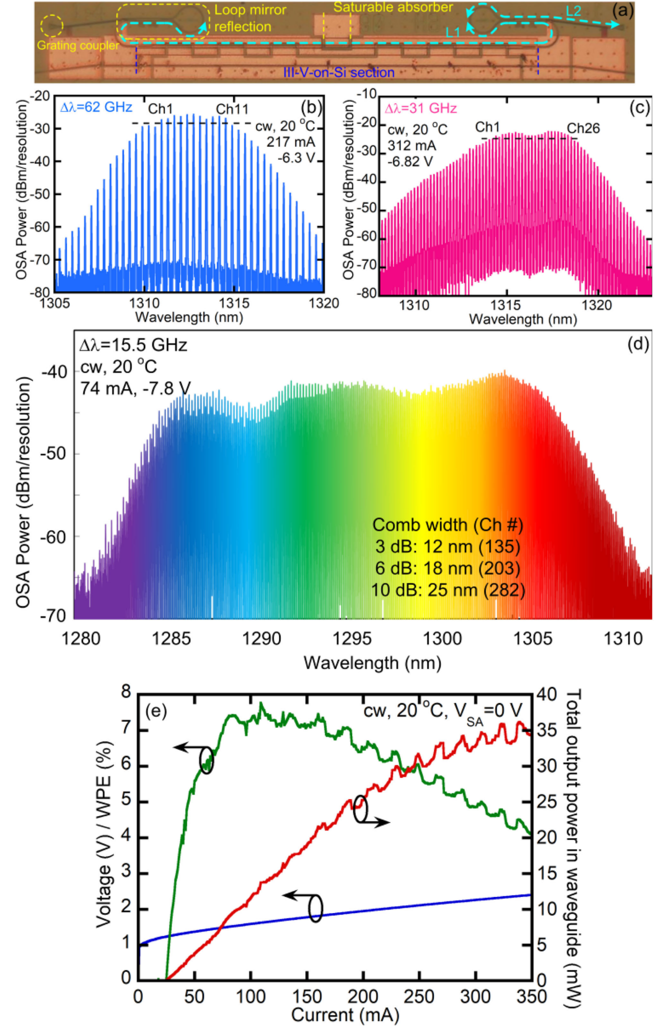

Fig. 3. (a) Top-view microscope image of a fabricated heterogeneous external-cavity QD comb laser and (b) its cw spectrum at 20 °C; and spectra of devices with 30 GHz channel spacing in (c) and 15.5 GHz in (d) where comb widths at different levels and corresponding channel numbers are labeled. (e) LIV characteristic of the device in (b) [24], [53].

shown in Fig. 3(a), the heterogeneous QD comb laser consists of two cavities: L1 and L2. L1 is a 2.6 mm-long cavity including a 1.4 mm-long SOA region, Si passive waveguide and two Si multimode interferometer (MMI)-based loop mirrors (50% reflectivity). A 180 μm-long SA at the center of SOA region promotes four wave mixing and leads to an effective $\text{FSR}_1 \sim 31.5$ GHz for L1. An external cavity (L2) is formed between the Si MMI-based mirror and the GC with a $\text{FSR}_2 \sim 63$ GHz. Its lasing spectrum at 20 °C in Fig. 3(b) exhibits 62 GHz spacing, slightly off the target of 63 GHz which is governed by the Vernier effect in Eq. 2:

$$\Delta\lambda = FSR = \left| \frac{FSR_1 \times FSR_2}{FSR_1 - FSR_2} \right| \tag{2}$$

When 217 mA current and −6.3 V bias were applied to the SOA and SA sections, respectively, 11 comb lines within 3 dB

power variation all show over 40 dB extinction ratio. Considering the symmetric laser cavity design, at least 10 dB GC loss, and 10% fiber-coupled power for spectral measurement, this laser is capable of providing two 11-wavelength comb streams (22 channels in total) where each channel is −9 to −6 dBm in power. A similar external cavity structure without SA, i.e., FSR_1 ∼15.75 GHz, generates a 31 GHz-spaced spectrum with 26 comb lines within 3 dB variation in Fig. 3(c). Without the impact from L2 cavity, a solitary cavity laser (FSR = 15.5 GHz) emits an record-broad comb spectrum in Fig. 3(d) [24]. A comb width of 12 nm to support 135 comb lines within 3 dB power variation represents over 70% improvement over typical comb width of ∼7 nm or less in the literature. 282 comb lines are supported in a 25 nm comb width if a 10 dB power variation is acceptable. We hypothesize that the ultra-wide comb width is the result of a unique combination of spatial hole burning, group velocity dispersion, linewidth enhancement factor, and four wave mixing [24]. Detailed laser physics studies and design optimization of laser efficiency are underway [56]. Prior to the 15–63 GHz designs, a 14-channel 100 GHz-spaced comb laser was also demonstrated previously, and each line supported error-free (BER 10^{-12}) external modulation at OOK 10 Gb/s which was limited by the high-speed instrument then [55]. This Vernier cavity effect decouples the dependence of channel spacing with SOA length, enabling reasonable single-line power with large room for improvement, and flexible channel spacing design with simple single-SA configuration. The low-loss and high-index-contrast Si platform also offers a broad class of non-grating reflector design choices, greatly simplifying external cavity implementation in contrast to devices on monolithic platforms.

Fig. 3(e) shows cw light-voltage-current (LIV) characteristic of the 60 GHz-spaced comb (Fig. 3(b)) at 20 °C stage temperature with zero bias to the SA. III–V mesa and Si waveguide dimensions are designed to result in a confinement factor ∼15% to the active region containing five InAs QD layers. Measured threshold current of 24.7 mA is typical and a minimal value of 9.2 mA from a similar design indicates a very low threshold current density of 165 A/cm^2, one of the best numbers for all heterogeneous III–V-on-Si lasers. After taking two equal outputs and at least −10 dB GC loss into account, about 35 mW total power in the Si output waveguide is conservatively estimated under 350 mA injection current. This means a wall-plug efficiency (WPE) around 7.5%. Our previous temperature-dependent studies on a solitary Fabry-Perot (FP) laser with eight InAs QD layers displayed a similar WPE at 20 °C, and only 30% WPE degradation at 100 °C with characteristic temperature T_0 as high as 333 K [26]. The most recent preliminary measurements of a comb laser at the project target of 50 °C showed error-free operation (BER 10^{-12}) of over 40 comb lines [57]. They validate the excellent high-temperature operation perspective as expected in QD gain medium.

As indicated by Fig. 3(b)-(d), power for individual comb line drops proportionally as the number of comb lines within 3 dB power variation range increases because similar active region reservoirs accommodate about the same number of injected carriers and the quantum efficiency is similar. Higher

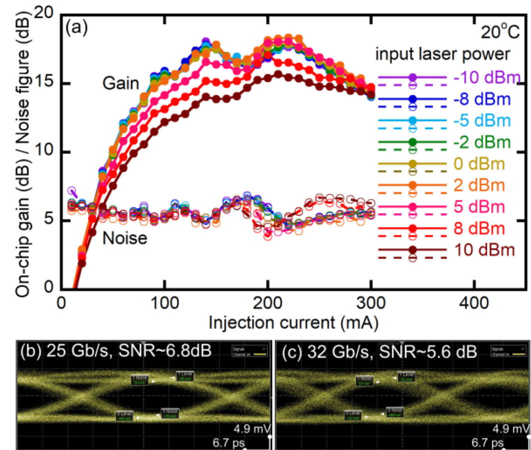

Fig. 4. (a) On-chip gain and noise figure of a heterogeneous SOA as a function of input laser power, and OOK eye diagrams at (b) 25 Gb/s and (c) 32 Gb/s [58].

laser efficiency is always desired, but the microring modulator also sets a threshold on incoming comb line intensity before a nonlinear effect kicks in as discussed later. Optical amplification is necessary, particularly after data modulation, in some scenarios of high link loss budget. The use of QD SOAs to boost multi-wavelength signals also benefits from its gain material because the strong confinement of charge carriers in the dots largely reduces channel cross-talk thanking to little cross-gain modulation and cross-phase modulation. Reduced chirp and larger saturated gain were also reported [25].

Fig. 4(a) shows our preliminary data on a heterogeneous QD SOA fabricated along with the MOSCAP microring modulators and QD APDs on the same chip [58]. The SOA design follows the similar principal as the gain section of the comb lasers. Over 18 dB on-chip gain for 1310 nm laser signal was extracted from this 1600 μm-long design under ∼220 mA pumping at 20 °C. Gain per length 11.25 dB/mm is on par or slightly better than several O-band InAs/GaAs SOAs on GaAs and Si substrate [27], [59]–[61]. The small change in the on-chip gain profile as a function of input power was noticed. No obvious saturation was observed when input power was 2 dBm or less. A maximal gain of 10 dB/mm could be maintained at laser inputs up to 8 dBm. Noise figures no more than 7.2 dB were also extracted based on the procedure in [62]. Abnormally high waveguide loss around 48 dB/cm (measured from a nearby reference Si waveguide without III–V on the top) in this particular fabrication run and some Fabry-Perot fringes due to reflections from I/O GCs could introduce some small variation for precise gain value extraction. Fig. 4(b) and (c) are eye diagrams with 6.8 and 5.6 dB SNRs when launching an OOK modulated signal at 1310 nm through the SOA at 25 and 32 Gb/s, respectively [58]. The SOA was pumped with 180 mA current during testing. The performance of this first generation heterogeneous QD SOA surpasses the project minimal goal of 10 dB on-chip and low-noise amplification at 25 Gb/s. The on-chip SOAs also lower power requirement on individual comb lines from the off-chip monolithic comb laser. Another potential advantage is to utilize different QD

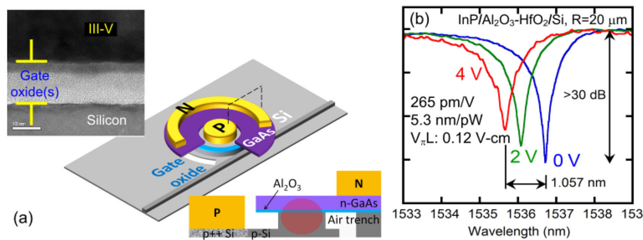

Fig. 5. (a) Schematic of a heterogeneous MOSCAP microring in bird eye's view and cross-sectional view, inset: a cross-sectional TEM image of the MOSCAP; (b) measured spectrum of a MOSCAP microring resonator with InP gate and Al_2O_3-HfO_2 gate oxide [32].

active region designs for the monolithic comb laser and heterogeneous SOAs to enable optimal spectral alignment between comb spectrum and gain peak. One architecture modification by recombining two deinterleaved 10-λ streams back into one 20-λ stream prior to SOA can utilize SOA gain more efficiently and reduce system power consumption. However, cross-talk could degrade signal integrity.

The progress of monolithic QD lasers on Si has been very rapid in the past 10 years as researchers [63] realized that the superior dislocation tolerance capability in QD gain media relative to their QW counterparts was like an effective vaccine for the pandemic. Instead of concentrating all the effort to develop different means to reduce the dislocation density, people grow QD materials on a lattice-mismatched substrate like Ge or Si to achieve enough gain to make decent lasers despite $\sim 10^8$ cm^{-2} dislocation density [50], [51], [63], [64]. Continuous development on both directions is certainly accelerating the maturity of the monolithic III–V-on-Si integration. Excellent comb lasers have been built on this platform and more details about using a monolithic comb laser in link demonstration are discussed in Section V. Due to space limit and several recent good reports on the monolithic QD lasers and amplifiers [47], [65]–[68], we will not cover more details of monolithic QD devices here.

B. Athermal Phase Shifter and Deinterleaver

Another main innovation in this DWDM platform is to fully take advantage of the heterogeneous MOSCAP [31] or sometimes called semiconductor-insulator-semiconductor capacitor (SISCAP) [33] for athermal and efficient phase tuning, and high-speed modulation [33], [69]–[71]. A cross-sectional transmission electron microscope (TEM) image in Fig. 5(a) inset exhibits such a structure consisting of a thin layer (e.g., ∼15 nm here) of the gate oxide sandwiched by III–V and Si materials. When an electric field is applied across MOSCAP, free electrons and holes around the semiconductor/oxide interfaces can be manipulated. As a schematic example in Fig. 5(a), placing the MOSCAP into a waveguide introduces plasma dispersion effect to the optical modes. Compared with the typical monolithic MOSCAP structure based on poly-Si/SiO_2/mono-Si [72], the heterogeneous one is not only much easier to fabricate, but also heavily favors more desirable III–V electro-optic effect [70]. Wafer bonding step removes the necessity to planarize the mono-Si surface through chemical mechanical polishing (CMP) which is inevitable to form the monolithic MOSCAP structure. ThusCMP-induced non-uniformity in waveguide thickness is avoided. On the other hand, III–V materials of interest (InP- and GaAs-based) have smaller conductive effective mass and larger carrier mobility for electrons than those of mono-Si and poly-Si [44]. It naturally leads to the adoption of n-type III–V as the gate and p-type Si as the base. This configuration co-incidentally matches with III–V epitaxial stack design convention for heterogeneous integration [36], [73]. Therefore, n-type InP- or GaAs-based material as a part of the III–V diode also serves as the gate in MOSCAP simultaneously to allow simple III–V epitaxial design, a shared ground terminal, and a compatible fabrication flow illustrated in Fig. 2. Small effective mass and higher mobility in III–V directly result in larger real part refractive index change for more efficient phase shift and smaller imaginary part refractive index for lower free carrier absorption (FCA). Lower optical scattering in mono-crystalline III–V material than that of poly-Si achieves further waveguide loss reduction. Choosing GaAs-based QD material over InP-based QW material in this platform further extends this benefit due to even higher electron mobility and smaller electron effective mass in GaAs [44]. Other electro-optic effects in III–V also contribute device performance positively [70].

This heterogeneous MOSCAP can be conveniently integrated in routing waveguide, resonators and MZIs, etc. Fig. 5(b) is the experimental spectrum of a 20 μm in radius MOSCAP microring resonator under 0, 2 and 4 V bias on MOSCAP [32]. n-InP was the gate material, and a ∼9.6 nm-thick gate oxide composed of a combination of high-quality high-k Al_2O_3 and HfO_2 enhances capacitance and subsequently plasma dispersion effect. Close to 1.1 nm resonance blue shift under 4 V forward bias proves its plasma dispersion effect rather than thermal effect, and translates to an efficient phase tuning rate of 265 pm/V and high tuning efficiency of $V_\pi L = 0.12$ V-cm in the C-band. As plasma phase tuning is a function of λ^2 [74], the same MOSCAP phase tuning efficiency and FCA will reduce by 40% from the C-band to O-band. But by replacing n-InP with n-GaAs, the same MOSCAP design will results in at least 40% improvement on phase tuning and another 22% down in FCA under a normal bias range <5 V [44]. Extremely low leakage current in tens of pA level (∼50 pA here) results in a phase tuning energy efficiency ∼5.3 nm/pW, at least 9 orders of magnitude better than the state-of-the-art numbers for thermal tuning [75] and carrier injection [76]. This ultra-energy efficient phase tuning immediately eliminates the power consumption in wavelength tuning/locking in proposed DWDM link when tuning within one channel spacing (120 GHz, 0.68 nm in the O-band) is needed. Its athermal nature also permits much smaller device spacing without thermal crosstalk.

In a proposed cascaded microring bank (either modulator or DEMUX) the physical microrings 1–10 do not necessarily need to match with comb lines λ 1–10. The control algorithm will match each microring resonance with a comb line closest to it. With negligible power compsution in static MOSCAP tuning, all microrings can also be pre-biased to allow blue and red shifts by a maximum of half channel spacing to accomplish

the initial match. On the other hand, the same MOSCAP tuner can be easily integrated into the on-chip heterogeneous comb laser to enable fine tuning of the comb spectrum as well. Furthermore, the same combination of Si and GaAs material system for the heterogeneous comb laser, deinterleavers and microring modulators leads to almost identical spectral response to the temperature change. About 77 pm/°C shift in the heterogeneous comb laser and MOSCAP microring modulator was measured in our lab. On-chip proximity and the same "walking" pace among components on the same chip demand little large tuning after initial match, and avoid using barrel shifting in the drivers. This MOSCAP phase tuner is of great use in correcting phase errors in the heterogeneous MOSCAP deinterleavers as well. Various deinterleaver designs such as 2nd/3rd order asymmetric MZIs (AMZIs), single, double, triple-ring assisted MZIs (RAMZIs) and cascaded 2nd order microring filters were explored [77], and a selective of them are discussed here. Unlike designs based on the energy-inefficient thermal tuners [78]–[81], each of our designs includes MOSCAP phase tuners integrated onto the delay paths such that any phase errors can be corrected to achieve high extinction ratio of nearby transmission passbands. The N_{th} order AMZI is modeled with a series of N MZIs whose individual transfer matrix can be described as $\Phi_{MZI} = \Phi_{cplr}(\kappa_2)\Phi_{delay}\Phi_{cplr}(\kappa_1)$[82], where Φ_{MZI} is defined in Eq. 3,:

$$\Phi_{MZI} = \begin{bmatrix} c_2(\lambda) & -js_2(\lambda) \\ -js_2(\lambda) & c_2(\lambda) \end{bmatrix} \begin{bmatrix} e^{-j2\pi n_g(\lambda)\Delta L_1/\lambda} & 0 \\ 0 & 1 \end{bmatrix} \times \begin{bmatrix} c_1(\lambda) & -js_1(\lambda) \\ -js_1(\lambda) & c_1(\lambda) \end{bmatrix} \quad (3)$$

The through and cross port transmission are respectively defined as $c_{1,2} = \sqrt{1-\kappa_{1,2}(\lambda)}$and $-js_{1,2} = -j\sqrt{\kappa_{1,2}(\lambda)}$, where $\kappa_{1,2}$ is the power coupling coefficient for each coupler, n_g is the group index and ΔL_1 is the path length difference that determines the FSR. Similarly, the RAMZI can be modeled by Eq. 4 [82]:

$$\Phi_{1RAMZI} = \begin{bmatrix} c_2(\lambda) & -js_2(\lambda) \\ -js_2(\lambda) & c_2(\lambda) \end{bmatrix} \begin{bmatrix} A^R(z)/A(z) & 0 \\ 0 & z^{-1} \end{bmatrix} \times \begin{bmatrix} c_1(\lambda) & -js_1(\lambda) \\ -js_1(\lambda) & c_1(\lambda) \end{bmatrix} \quad (4)$$

where $A^R(z) = \sqrt{1-\kappa_r} + (e^{j2\pi n_g(\lambda)\Delta L_1/\lambda})^{-2}$, $A(z) = 1 + \sqrt{1-\kappa_r}(e^{j2\pi n_g(\lambda)\Delta L_1/\lambda})^{-2}$, and κ_r is the ring coupling coefficient. Fig. 6(a) and (b) show the deinterleaver response for the 2nd order AMZI and 1-ring RAMZI, respectively. The dashed lines indicate the extreme case for a π phase error in a path length, causing unusable extinction ratio and much narrower passband. The solid lines indicate the corrected response by use of the MOSCAP phase tuners which are highlighted in purple in respective schematic of Fig. 6(a) and (d) insets. The FSR of a deinterleaver is twice the intended channel spacing where $FSR = \lambda_{target}{}^2/n_g/\Delta L$. λ_{target} is the vacuum wavelength at the center spectral window, and ΔL is the base optical path length difference between the upper and lower arms. Therefore, a channel spacing of 65 GHz for the 2nd order AMZI requires ΔL

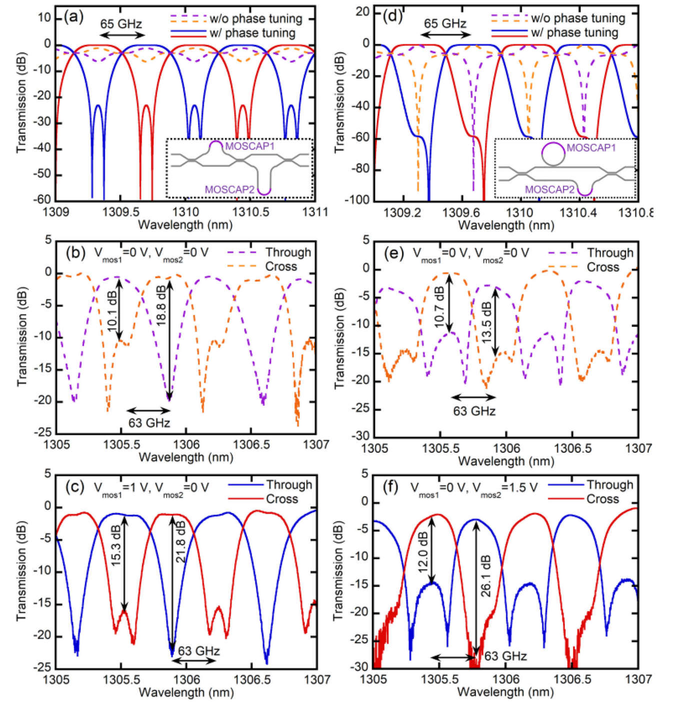

Fig. 6. Simulated deinterleaver transmission response with (solid) and without (dashed) MOSCAP phase tuning for (a) 2nd order AMZI design and (d) 1-Ring RAMZI both with 65 GHz channel spacing and assumed π phase corrections; and their respective measured transmission responses from (b) (e) as-fabricated and (c) (f) corrected phase from one phase tuner. [77].

= 610.5 μm for a calculated group index of $n_g = 3.78$. For the 1-ring AMZI, the ring circumference sets the channel spacing of 65 GHz and in this case $L_{ring} = 1200$ μm, $\kappa_r = 0.89$, and $\Delta L_1 = 600$ μm. The applied voltage needed for an appropriate π phase shift depends on the capacitance of the MOSCAP, hence the choice of dielectric as well as thickness is important.

Fig. 6(b) and (c) are the measured responses for a 2nd order MOSCAP AMZI deinterleaver before and after phase correction. The extinction ratio of the through channel was improved from 10.1 to 15.3 dB while the cross channel increased from 18.8 to 21.8 dB by only applying 1 V bias on the first MOSCAP tuner. An average 1 dB passband bandwidth of 48 GHz for the through and cross port was obtained after phase correction, easily accommodating the 2 GHz channel spacing offset between design (65 GHz) and experiment (63 GHz). The ILs before and after MOSCAP tuning are ~0.4 and 1.0 dB, respectively. Fig. (e) and (f) are similar comparison on a 1-ring RAMZI before and after phase correction. The extinction ratio of the through channel was improved from 10.7 to 12.0 dB while the cross channel improved from 13.5 to 26.1 dB upon 1.5 V bias on the 2nd MOSCAP. 1 dB passband bandwidth is 29 GHz averagely and uniformity between through and cross transmission is also improved after tuning [77]. Further improvement on extinction and uniformity was measured when more than one phase tuners were controlled synergistically [35]. Lower IL is expected when fabrication process is refined to reduce passive Si waveguide loss which was abnormally high (>10 dB/cm) in this fabrication run.

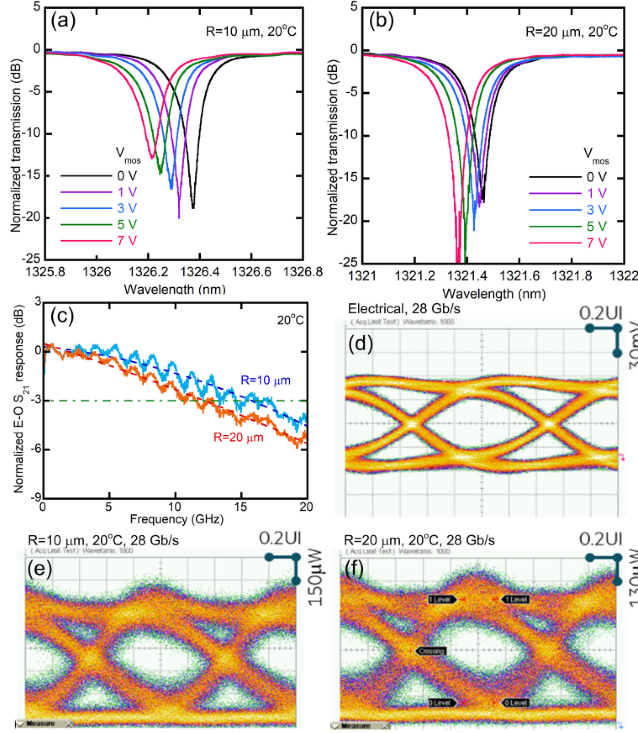

Fig. 7. Normalized experimental spectra for various applied MOSCAP voltages for (a) 10 μm and (b) 20 μm in radius devices at 20 °C, and (c) normalized S21 characteristic, and (d) electrical OOK driving signal diagram for respective optical diagrams at 20°C in (e) and (f) [34].

C. High-speed Modulators

The monolithic poly-Si/SiO_2/mono-Si MOSCAP structure enabled the first ever Si modulator with modulation bandwidth exceeding 1 GHz [83], and a modified design has been successfully commercialized to deliver excellent OOK modulation at 40 Gb/s and beyond [72]. A recently reported heterogeneous counterpart exhibited promising 32 Gb/s OOK operation under a pre-emphasis signaling [69], and another MOSCAP design demonstrated 30 GHz bandwidth [71]. Nearly all demonstrated high-speed MOSCAP modulators so far are based on MZI configuration which is not suitable for DWDM application here as discussed in Section III.

Shown in Fig. 5(a), a microring-type heterogeneous MOSCAP high-speed modulator has been developed in our lab [33], [34]. It was fabricated on the same chip as heterogeneous QD lasers, amplifiers, and PDs as illustrated in Fig. 2. ~20 nm Al_2O_3 was used as the gate oxide and device radius range is 10-25 μm. Fig. 7(a) and (b) are measured spectra of the devices in 10 and 20 μm radius as a function of MOSCAP bias V_{mos} at 20 °C, respectively. All spectra were normalized to the lowest optical loss point of the spectrum with $V_{mos} = 0$ V only, indicating no IL change with MOSCAP control. Similar to Fig. 5(b), the blue shift of resonance wavelength and reduction in quality factor (Q) with increasing bias are due to plasma dispersion effect-resulted model index change in both real and imaginary parts, respectively. The 10 μm radius one operated around the critical coupling regime before additional FCA perturbation while the 20 μm one started with under-coupled regime. Due to relatively thick Al_2O_3 gate oxide, $V_\pi L$ for both devices is around 1 V-cm, over 8× larger than that of a previous one using a thin Al_2O_3-HfO_2 gate oxide for stronger plasma dispersion effect [32].

TABLE I
STATIC AND DYNAMIC PARAMETERS OF MOSCAP MICRORING MODULATORS

R (μm)	FSR (nm)	Power coupling	Loss (cm^{-1})	Q_{tot}	f_{RC} (GHz)	f_Q (GHz)	f_{3dB} (GHz)	ER (dB)
10	7.518	5.5%	13	8143	27	17.9	15.2	5.6
20	3.658	14.7%	9.85	8130	14	18.1	12.6	7.9

For all capacitive devices, the RC-time constant is a critical design tradeoff for the high-speed dynamics. A single-transverse mode waveguide design (500 μm in width here) is important for high signal integrity as well as small capacitance. A deeply etched trench (Fig. 5(a)) in the slab side close to III–V metal contact is implemented to confine majority of the dynamically manipulated MOSCAP region to the microring cavity only [31]. The RC-time constant is relatively independent from the microring radius as capacitance and resistance both change proportionally but in the opposite direction. Fig. 7(c) shows the S_{21} curves for the two devices. The ripples are likely from the setup and not intrinsic to the device as they were present during calibration. The curves were obtained at a detuning that maximizes optical modulation amplitude (OMA) or DC value of S_{21}. A careful study on modulation signal quality vs. wavelength detuning will be necessary to understand how accurate the phase control needs to be. Corresponding 3 dB bandwidths are between 13–15 GHz and smaller device has a slightly higher bandwidth. Spectral fitting could help to break down the photon lifetime and RC-time constant bandwidths. Taking 10 μm radius one as example, its measured 3 dB bandwidth is close to calculated photon lifetime bandwidth around 18 GHz and further away from RC-time constant bandwidth around 27 GHz. However, the situation is different for 20 μm or larger radius one where RC-time constant is the limiting factor. Decent large-signal performance up to 28 Gb/s of OOK for all device dimensions were measured. An arbitrary waveform generator (AWG) generated electrical signal with PRBS15 pattern in Fig. 7(d) which was boosted up to peak-to-peak swing (V_{pp}) of 4 V by a RF amplifier. Other than compensating cable and connector loss, no pre-emphasis signaling from AWG was applied to the modulator. Fig. 7(e) and (f) show open eye diagrams with corresponding extinction ratio of 5.6 and 7.9 dB for 10 and 20 μm radius devices at 20°C, respectively. Measured off-resonance IL is negligible under static operation and around 1.5-2 dB during dynamic modulation. The extracted parameters are summarized in Table I. Smaller microring suffers more from waveguide sidewall-induced scattering loss, so smaller power coupling is necessary to realize a decent quality factor.

Lower driving voltage (i.e., power consumption), lower dynamic IL and higher bandwidth are attainable by reducing device dimension, employing thinner or higher dielectric gate oxide, and improving doping profile for lower device resistance [34].

Temperature-dependent characteristic of the heterogeneous MOSCAP microring modulators were studied as well. With a

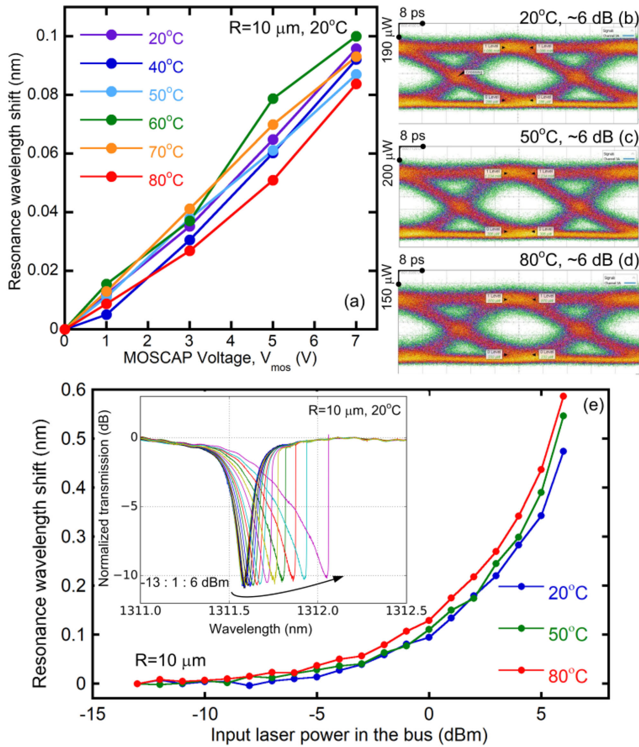

Fig. 8. (a) Resonance wavelength shift vs. MOSCAP bias voltage for different stage temperatures. (b-d) 25 Gb/s optical eye diagrams at 20, 50 and 80 °C, respectively. (e) Resonance wavelength shift vs. input laser power in the bus waveguide at 20, 50 and 80 °C. Inset: Sample spectra showing asymmetric transmission around resonance. Wavelength was swept from left to right [34].

measurement error of 10 pm, the static wavelength tuning efficiency shows little to no degradation between 20 to 80°C in Fig. 8(a). This is further confirmed with 25 Gb/s open eye diagrams (Fig. 8(b)-(d)) from 10 μm radius device at 20, 50 and 80°C, respectively. The extinction ratio ~6 dB at all temperatures demonstrates desirable operation robustness. The eye diagram at 80°C shows some excess noise due to momentary optical coupling instability. The operating wavelength is well detuned from the bandgap of GaAs and Si, thus changes in modulation efficiency from changing bandgap with temperature is weak.

The nonlinear effect in microring was also studied to identify the threshold for bi-stable operation with increasing input laser power [84]. It is critical to the designs of comb laser, SOA and overall architecture. For the 10 μm radius device, at 20°C the resonance wavelength starts to red shift for 20 pm to become asymmetric at -5 dBm (Fig. 8(e) inset), and at 80°C it is nearly -7 dBm (Fig. 8(e)), both refer to the tunable laser output power coupled into the bus waveguide. We also observed that the modulator with 10 μm radius showed a slightly larger drift for a given optical power compared to modulators with radii 20 and 25 μm. The use of a pulsed comb source further reduces the onset of this thermal drift by ~3 dB. This indicates that there is a trade-off between maximum permissible laser power per channel and the modulator FSR. If the comb laser in Fig. 3(b) is employed as a dual-output source in the link, it is indeed necessary to place the SOAs after the modulator banks to avoid nonlinearity-induced variable resonance shift in microring modulators. This situational design flexibility is also a clear advantage of the heterogeneous integration without incurring fabrication or packaging complexity or optical losses.

D. Quantum-dot Avalanche Photodetector

PDs were one of the earliest demonstrated devices in several heterogeneous III–V-on-Si platforms [85]–[88]. Since bulk InGaAs layer is the typical absorption layer, heterogeneous on-chip TRx integration requires bonding at least two separate III–V epitaxial structures for optical gain and absorption plus more complex post-bonding III–V fabrication flow. In our case co-integration of GaAs-based QD optical gain material and InP-based InGaAs detector material certainly will make the fabrication more challenging due to two different III–V material systems. Fortunately, high-performance waveguide-type QD APDs based on the identical QD laser/SOA epitaxial structure were developed recently to avoid any fabrication overhead associated with new III–V material involvement [89], [90].

Fig. 9(a) exhibits the static performance of a 3 μm×30 μm device. The dark current density as low as 3.3×10^{-7}A/cm^2 from 10 pA dark current at -1 V bias is among the lowest dark current ever reported for a III–V-on-Si PD [89]. Such low dark current was also observed in the monolithic InAs QD PDs [91]. It is one of the prerequisites to obtain high sensitivity, and there is still room to further reduce it as the present main contributor is the surface leakage rather than bulk material. The absorption coefficient of the active region with 8 QD layers is about 900 cm^{-1} at 1310 nm. Photogenerated carriers in QDs can escape either through thermionic emission or tunneling under high reverse bias. Monte Carlo simulations have shown that under high applied electric fields, there is a high likelihood that carriers that escape from QDs will travel in the continuum without being captured by another QD until reaching the electrical contact [92]. This is due to the higher average energy of the escaped carriers under high electric field. This means higher quantum efficiency, as well as impact ionization rates, for APDs at a high bias. TE- and TM-polarization dependent responsivities were observed by maximizing or minimizing coupled input light from a TE-polarized grating coupler. Under the unity gain at -4 V where the photocurrent stays flattest, the corresponding responsivity for TE and TM modes is 40 and 7 mA/W, respectively. Low responsivity at 1300 nm is due to strong photogenerated carrier confinement in the ground state and small overall optical confinement to the QDs. Responsivity can be enhanced through adding more layers of QDs, increasing device length, or forming a resonance cavity. Unequal absorption for TE and TM modes comes from the difference in quantum confinement in the plane and the growth direction of the QDs. Higher reverse bias led to exponentially increasing photocurrents due to avalanche gain effect which partially occurs inside the InAs QDs [93] and the GaAs spacer layers [94]. Extremely high gains up to 150 and 355 were measured for respective TE and TM modes around the breakdown voltage of -18 V at room temperature. The avalanche effect strongly depends on the interaction or coupling between the wave functions. Since under TM mode photocurrent

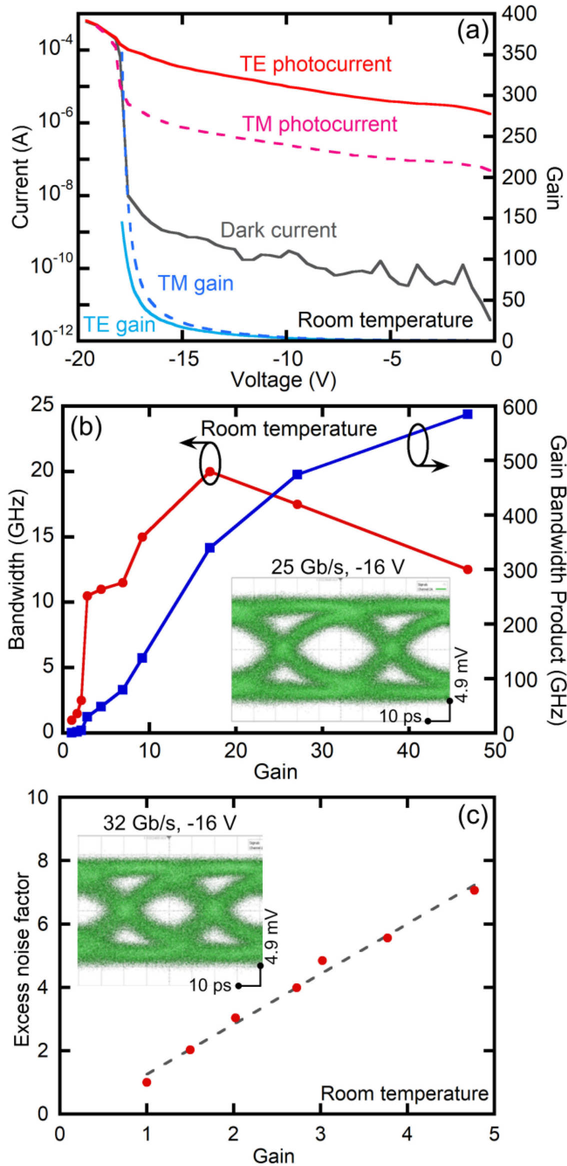

Fig. 9. (a) Dark current, photocurrent, and gain as a function of bias voltage for TE and TM input optical mode polarizations for a waveguide QD APD, (b) room temperature bandwidth and GBP, and (c) excess noise factor of the same device as function of gain. Insets: measured OOK eye diagrams at 25 and 32 Gb/s [89].

wave function couples weakly between QDs, this high electric isolation facilitates the avalanche multiplication process, leading to a higher gain in TM mode [95]. Avalanche gain process was still measurable up to 60 °C in an earlier batch of devices [90].

The RC-time constant-limited 3 dB bandwidth was as high as 20 GHz under the TE-polarized input and -15 V bias (gain M = 17) in this 3 μm×30 μm device (Fig. 9(b)). Bandwidth started decreasing under higher bias voltage due to longer avalanche buildup time, but gain-bandwidth product (GBP) reached a record-high value of 585 among all reported QD APDs to our best knowledge [89]. Higher GBP for TM-polarized light input is expected owing to even higher TM gain. Without an integrated TIA, large signal characterization at bias of -16 V was carried out under a modulated OOK input at 1310 nm with optical power of −6 dBm and PRBS15. Insets in Fig. 9(b) and (c) are experimental eye diagrams at the project target of 25 Gb/s and instrument-limited 32 Gb/s, respectively. The corresponding SNRs are 3.4 and 3.2, showing its capability to serve as high-speed receiver in this heterogeneous DWDM TRx [89].

The excess noise factor under the TE-polarized input was measured and shown in Fig. 9(c) in order to extract k factor, the ratio of hole and electron impact ionization coefficient. The extracted k factor is about 0.14 [89], which is smaller than III–V counterparts such as APDs based on InAlAs ($k = 0.2$), InP ($k = 0.3\sim0.4$), GaAs and AlGaAs ($k = 0.4\sim0.5$), but higher than InAs ($k\sim0$) [96]. It indicates that avalanche multiplication takes place in both the InAs QDs and the GaAs spacer layers. Ultra-low noise is unlikely because the absorption of light inside the multiplication region adds extra gain fluctuations unless a separate absorption, charge, and multiplication (SACM) structure is employed. TE and TM mode sensitivity measurement is under way to study its impact to the link loss budget, and on-going design optimization includes further improvement on device robustness and development of a SACM QD APD structure to reduce the breakdown voltage.

E. SiGe Avalanche Photodetector

As the flagship high-sensitivity receiver candidate in our overall energy-efficient DWDM photonics roadmap, SiGe APDs are also being thoroughly studied in our lab. Ge is a CMOS-compatible material and well suited for efficient light absorption in all traditional telecom windows. Extremely small k factor around 0.01–0.02 for Si versus $k\sim0.9$ for Ge also enables a convenient and desired SiGe SACM APD design [99] as long as a high-quality Ge/Si interface quality is resulted after the Ge epitaxy. A vertical p^+-p^--i-n^+ SACM structure was developed and shown by the SEM cross-sectional image and electric field schematic both as insets of Fig. 10(b) [39]. On top of the 220 nm-thick n+ Si device layer, 150 nm-thick intrinsic Si (i-Si) was grown, followed by Boron implantation into 50 nm-deep surface area as p- charge layer and epitaxy of 400 nm-thick p+ Ge. While doped Ge increases the dark current density ($\sim$1 mA/cm^2 at −2 V, 20 °C), it concentrates high electric field perpendicular to Si plane in the i-Si layer to fully take advantage of low excess noise carrier multiplication in Si. The majority holes respond within the relaxation time in p+ Ge layer, making electrons the uni-traveling carrier transport to the bottom n-type cathode at overshoot velocity to achieve high speed. Proper design in the p- Si charge layer and thin i-Si multiplication layer further reduce the breakdown voltage to −10 V. Another novel three-terminal design based on the same epitaxial SiGe structure but building high electric field along in-plane direction resulted in an even lower breakdown voltage of -6 V [100]. Similarly low operation voltages of −7 V and −4.9 V were also reported on Ge APDs [101], [102]. They are significantly smaller than typical values of tens of volt seen in III–V APDs, and subsequently reduce practical application barrier of SiGe APD in silicon photonics PICs. More design and characterization details can be found in [39], [100].

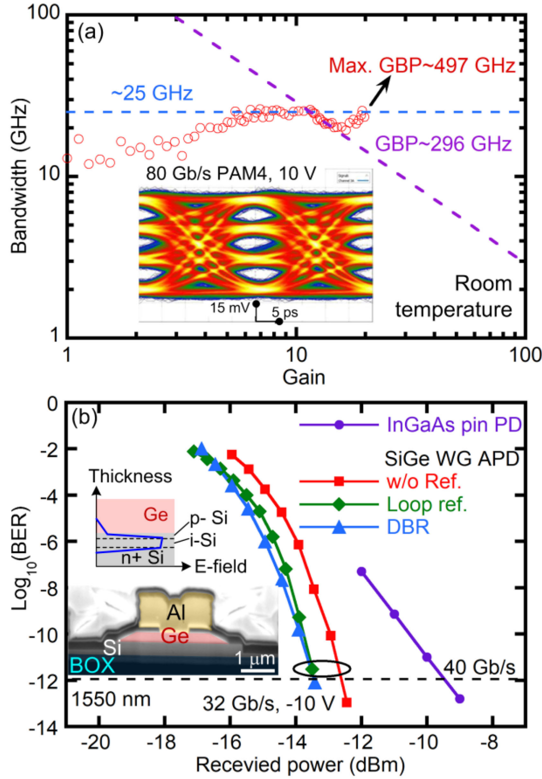

Fig. 10. (a) Bandwidth vs. gain of the SiGe APD with loop reflector and inset: measured 80 Gb/s PAM4 eye diagram [97]. (b) BER characteristic of SiGe APD with and without reflector and a reference commercial InGaAs pin PD [98].

A recent design optimization is to integrate a broad-band Si reflector, either a DBR [103] or loop-mirror reflector design [98], right after the SiGe device region to effectively reduce the required device length by half. For a typical 4 μm$\times$10 μm Ge mesa design, short cavity ensures a small RC-time constant but suffers from relatively poor responsivity around 0.75 A/W [39]. Upon a reflector is added at the mesa end, the reflector-induced dual absorption path and interference between incoming and reflected optical modes enhance the responsivity and internal quantum efficiency by 1.49$\times$ to 1.12 A/W and 89.6%, respectively [98]. It noted that all SiGe performance was measured at 1550 nm due to input GC design, and better performance is expected at 1310 nm for stronger Ge absorption.

Fig. 10(a) plots 3 dB bandwidth of the same device as a function of gain. When reverse bias is less than -9.6 V, i.e., M<6, bandwidth increases with gain (i.e., reverse bias) due to extending depletion region width in the Ge absorber and decreasing junction capacitance. Then it reaches a constant around 25 GHz in medium gain region (6<M<12) when Ge is fully depleted. Further rising of the gain (12<M<17) starts reducing bandwidth because of longer avalanche build-up time, resulting a saturated GBP of $\sim$296 GHz. In the high gain region (17<M<20), the 3 dB bandwidth picks up again due to high current density-induced space charge effect [105], [106]. Up to 497 GHz was obtained at gain of 19.4 in a loop reflector-assisted device [98]. An open 80 Gb/s PAM4 eye diagram with -10 dBm input in Si waveguide and a RF amplification (not TIA) to boost photocurrent was measured in Fig. 10(a) inset [97]. The device's low noise characteristic leads to outer optical modulation amplitude (OMA) of 70.48 mV and transmitter dispersion eye closure quaternary (TDECQ) of 0.99 dB. Due to limitation in our bit-error rate tester (BERT), only sensitivity at 32 Gb/s OOK signaling was characterized and compared among SiGe APD designs without reflector, with loop-mirror reflector, with DBR, all under -10 V bias, plus a commercial InGaAs p-i-n PD as reference. Fig. 10(b) exhibits a sensitivity of -13.4 dBm at BER of 10^{-12} in reflector-assisted SiGe APD designs. This translates to 1 dB and 3.9 dB improvement over the SiGe APD without reflector and InGaAs p-i-n PD, respectively [97].

The temperature robustness was also studied carefully on our SiGe APDs, and the same 4 μm$\times$10 μm design without reflector was selected as the primary candidate. The ratio of breakdown voltage change as a function of temperature, $\Delta V_{bd}/\Delta T$, refers to the gain-temperature stability. Compared with SACM APDs made by InAlAs-InGaAs and InP-InGaAs material systems and having thicker multiplication and depletion widths, SiGe APD demonstrates excellent stability as breakdown voltage only changes from -9.9 to -10.2 V between 23 and 90 °C, resulting in significantly smaller $\Delta V_{bd}/\Delta T = 4.2$ mV/°C [104]. Both the thin Si multiplication (100 nm) and depletion (150 nm) layers in this p^+-p^--i-n^+ SACM structure contribute to good gain-temperature stability. Free carriers drifted into very high electric field in the i-Si multiplication layer quickly gain acceleration and have very small probability to scatter with phonons before reaching ionization threshold energy. Therefore higher temperature doesn't hugely impact the ionization coefficient and subsequently gain multiplication efficiency. Gain over 15 was obtained in all temperature settings from 23 to 90 °C [104]. Dark current increases constantly at higher temperature like typical SiGe p-i-n detectors do because Shockley-Read-Hall recombination mostly occurring in the traps at the Si/Ge interface is the primary source of dark current. But a favorable consequence of temperature rise is bandgap reduction in Ge. Smaller bandgap enhances absorption coefficient a and then internal quantum efficiency QE. Eqs. 5 and 6 describe the temperature dependence of these two parameters [104].

$$a(T) = [C(T - T_0)]^2 + a(T_0) \tag{5}$$

$$QE(T) = 1 - \exp\{-[C^2(T - T_0)]^2 + a(T_0)]L\} \tag{6}$$

Here C is a fitting parameter, T_0 is the initial temperature and L is absorber length. Theoretical fitting agrees with measurement very well in Fig. 11(b). Internal quantum efficiency approached 100% when temperature was 60 °C or higher. In addition to less than 0.3 V change in the breakdown voltage, device bandwidth and GBP were only slightly lower at elevated temperature with slow degradation rates of -23.3 MHz/°C and -687 MHz/°C, respectively. The minimal bandwidth change and enhanced responsivity at high temperature enlarged eye opening. Both PAM4 and NRZ OOK signaling at different gain setting and temperature were measured. Eye diagrams of 30, 60 and 90 °C at 32 Gb/s NRZ OOK signaling with PRBS9 are shown in Fig. 11(b) inset. The same signal integrity is maintained as

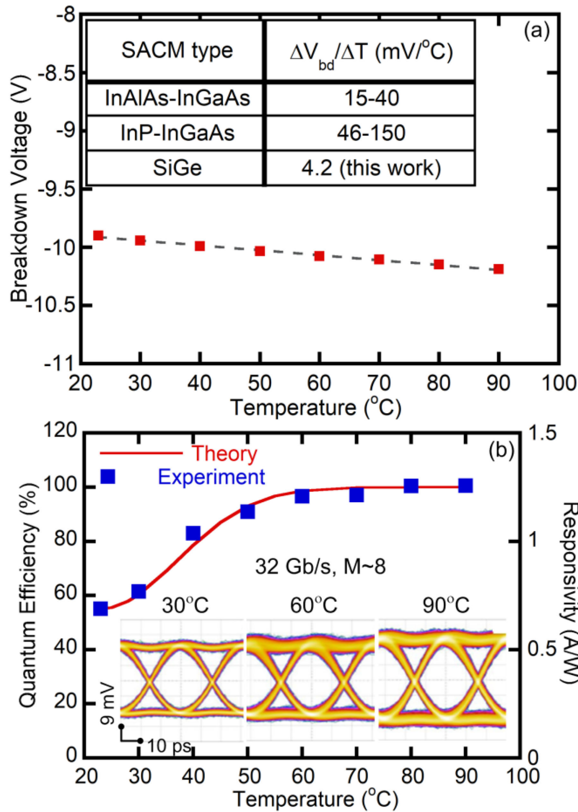

Fig. 11. (a) SiGe APD breakdown voltage vs. temperature, inset: table of gain stability among different SACM APD designs. (b) SiGe APD internal quantum efficiency and responsivity vs. temperature. Inset: OOK eye diagram at 32 Gb/s at 30, 60 and 80 °C [104].

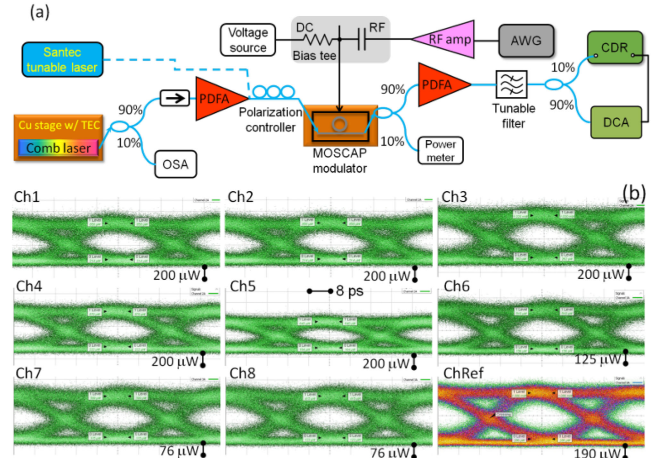

Fig. 12. (a) Transmitter optical link experiment diagram, and (b) OOK eye diagrams at 25 Gb/s for each of the eight comb wavelengths and one for reference source. Extinction ratios in order: 6, 6, 5.9, 5.9, 5.9, 5.1, 5.4, 5.3 and 6 dB [53].

temperature rises because larger eye height from higher photocurrent compensates the higher shot noise from higher total of photocurrent and dark current.

High sensitivity, high speed, robustness, low bias voltage and CMOS compatibility from this SACM-type SiGe APD offer plenty of merits to enhance system performance and integration density. It indeed requires fabrication process development to integrate SiGe APD on the heterogeneous III–V-on-Si platform as schematically shown in Fig. 2. Detailed process integration and TRx design is under way.

V. DWDM Link Demonstration

With on-going efforts to polish the full DWDM TRx design and fabrication, preliminary link demonstrations based on discrete components are discussed here. All discrete heterogeneous devices were built on the same platform, so they can be integrated seamlessly on the same chip. In a transmitter link testing shown by the diagram in Fig. 12(a), the same device in Fig. 3(a) was used as the DWDM source [53]. 10% of its single-side output power was for spectral monitoring, and 90% went through an optional isolator and then was amplified by a praseodymium-doped fiber amplifier (PDFA). A TE-polarized full comb stream was launched into a single MOSCAP microring modulator with 10 μm in radius because cascaded microring modulator array on the same chip failed to operate unfortunately due a mask error. So only one wavelength matching the modulator resonance got encoded with the PRBS15 NRZ OOK signal. 90% of the modulated signal was amplified again before reaching a tunable optical filter to remove un-modulated wavelength channels. Two PDFAs compensated about -30 dB link loss primarily from GC losses of the comb laser chip (−10 dB) and modulator chip (−7 dB) plus another −5 dB IL of the tunable filter. A clock data recovery (CDR) was used to generate trigger for the digital communication analyzer (DCA). In order to evaluate the modulated signal quality of eight individual comb wavelengths, the stage temperature of the comb laser chip was fixed at 20.5 °C and the modulator chip sits on a stage whose temperature was varied from 11.7 to 46.1 °C to tune the same modulator resonance sequentially to a certain wavelength in the incoming comb stream. A high-end single-mode tunable laser (Santec TSL-510) was used as a reference source to benchmark the comb wavelengths.

Under 253 mA current injection to the device gain region and −7 V reverse bias to the SA region, a heterogeneous comb laser emitted ten wavelengths within 4 dB power variation and with over 40 dB suppression to undesired fundamental cavity modes (spectrum not shown here). Eight of them were used in a link test [53]. The eye diagrams at 25 Gb/s from using each wavelength Ch 1-8 as optical carriers are exhibited in Fig. 12(b). Open eye diagrams are visible in each case, and their respective extinction ratios are: 6, 6, 5.9, 5.9, 5.9, 5.1, 5.4, and 5.3 dB, comparable to the value of 6 dB by using the reference laser source. A typical BER of 1×10^{-10} or better was measured. Eye diagrams for the comb laser appear slightly noisier mostly due to extra noise from the first PDFA and degraded optical SNR, rather than RIN from the comb source. Among all active optical building blocks, the laser power consumption usually dwarfs that of the modulator and detector. The total power consumed by this laser was 643.4 mW, including portions in gain and SA sections.

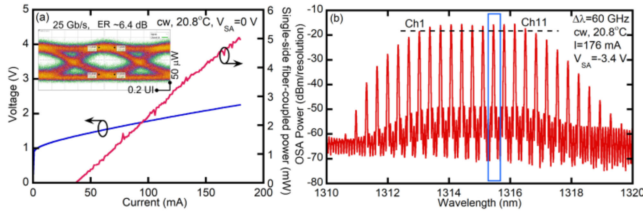

Fig. 13. (a) LIV characteristic of a monolithic QD modelocked laser on Si without bias on SA at 20.8 °C, inset: OOK eye diagram at 25 Gb/s; (b) comb spectrum from device in (a) under an ideal bias condition.

Given its symmetrical dual lasing outputs, only half of it, 317.2 mW, should be counted here. The MOSCAP microring modulator contributed about 0.5 pJ/bit energy consumption based on $1/4CV_{pp}^2$. Thus a link energy efficiency of 2.1 pJ/bit is achieved without taking PDFA power consumption into account. If we were taking advantages of all ten wavelengths per laser output, two equal outputs, and maximal modulator speed at 28 Gb/s, an aggregated bandwidth of 560 Gb/s and total energy efficiency of 1.6 pJ/bit would likely be obtained.

While not being illustrated in Fig. 1 to avoid confusion, a similar DWDM TRx configuration based on an off-chip QD comb source is also convenient to realize if separate temperature control on comb laser is necessary. For example, a monolithic InAs/GaAs QD comb laser on III–V native [21], [22] or Si [107] [23] substrate can be employed to feed multi-wavelength cw signal into a heterogeneous TRx chip with all the components in Fig. 1 except the on-chip comb laser which can be replaced by a broad-band optical input and a 1×2 optical power splitter. To prove the concept, here a 2730 μm-long dual-output monolithic QD modelocked laser on Si was designed to be a fourth-order colliding pulse modelocked configuration for 60 GHz channel spacing [54]. Two SA sections are placed symmetrically at the one of the fourth position of the whole cavity. Compared to the fundamental 60 GHz-spaced modelocked configuration of a 682.5 μm-long cavity with one SA placed close to the facet, the effective improvement from this high-order harmonic design is the increased output power as the cavity length is $4\times$ longer for more gain and decreased thermal effect favorable for the stable ground state lasing. The lasing active region was formed in a dots-in-a-well structure, and more design and fabrication details could be found in [54]. Fig. 13(a) shows device LIV characteristic at a stage temperature of 20.8 °C when SA was not biased. The device started cw lasing at 37.8 mA and outputted 5 mW from one facet into a lens fiber. Comb spectrum at an ideal bias condition of 176 mA to the gain section and -3.4 V to the SA region was displayed in Fig. 13(b). 11 of 60 GHz-spaced channels within 3 dB power variation were available for link test and Ch 8 was selected as its matching with a microring modulator resonance. The same link testing setup in Fig. 12(a) was used but only PDFA #2 compensated excess I/O losses from edge coupling of laser output and two GCs in MOSCAP modulator chip due to unavailability of PDFA #1 then. Similar to ones in Fig. 12(b), an open eye diagram with 6.4 dB SNR in Fig. 13(a) inset indicated sufficiently low RIN. Average single line RIN of −133 dB/Hz was reported in a similar device with 20 GHz repetition rate [54].

In addition to the transmitter demo using home-made comb lasers and MOSCAP microring modulator, we also conducted more link tests by using each of 10 comb lines from a similar heterogeneous comb laser, a commercial $LiNbO_3$ modulator and a home-made surface-normal SiGe APD to achieve an aggregated bandwidth of 160 Gb/s [108]. SNR from each eye diagram was measured to be 4-5 dB. 16 Gb/s/λ NRZ OOK modulation rate was limited by relative poor responsivity of the surface-normal SiGe APD since its thin absorption layer was primarily designed for waveguide-type devices. Comparable results were obtained by swapping SiGe APD with a heterogeneous QD APD.

All these attempts validate the concept of a DWDM TRx link in Fig. 1 and functioning Tx and Rx performance. Aggregated link loss from I/O GCs (7–10 dB each) and tunable optical filter (5 dB each) skyrocketed to a level of more than 40 dB when we tried to connect home-made laser, modulator and APD (either SiGe or QD) chips together. Thus, at this moment we were not able to close the entire TRx link with a BER of 10^{-10} or lower due to accumulated ASE noise from multiple amplifiers between home-made chips. Link loss budget and energy efficiency calculation below further unfold how significant improvement of the system performance could be when they are all integrated in one PIC chip.

The table in Fig. 14 lists target optical loss of each element in the proposed DWDM link based on the in-house fabrication capability. Lower loss is for sure when the chip is fabricated in a quality foundry. Depending on choice of on-chip or off-chip comb laser, link loss budget of any one channel can be summed up in Fig. 14. 1D (2D) GC coupling includes −2 (−4) dB GC loss and additional -2 dB loss of a detachable fiber connector [109]. Lossless 1×2 splitter refers to dual output configuration of a 20-λ comb laser without needing a separate 1×2 splitter with -0.5 dB IL. IL of the MOSCAP microring modulator includes dynamic IL and the NRZ OOK modulation loss. APD sensitivity of -20 dBm at 25 Gb/s and heterogeneous SOA gain determine minimal power of each 20 comb lines. SiGe APD is used here to calculate energy efficiency which is 40 fJ/bit at 25 Gb/s [39]. In the first scenario (S1), 5% WPE is assumed for both on- and off-chip comb lasers, and a booster SOA is followed each 10-ch. modulator bank to provide 10 dB gain at a cost of 60 mW dissipated electrical power based on our experiment. A 5 μm in radius MOSCAP microring modulator with 15 nm-thick Al_2O_3 gate oxide only needs aV_{pp} of 2 V for 25 Gb/s operation, and consumes 2 mW modulator power (i.e., 80 fJ/bit) based on the calculation. Negligible power consumption for MOSCAP phase tuning is assumed. A total of -20.6 dB link budget, a 420 fJ/bit energy efficiency and minimal −9.4 dBm power from each comb line are calculated for a fully heterogeneous integrated DWDM TRx. Additional edge and GC coupling and a 1×2 optical power splitter when launching an off-chip comb light to modulator banks add -6 dB more loss, therefore energy efficiency and comb line power of off-chip source option are increased to 580 fJ/bit and −3.4 dBm, a power achievable in the lab at room temperature already. In the second scenario (S2), all GC-based I/Os on the heterogeneous TRx chip are replaced with edge

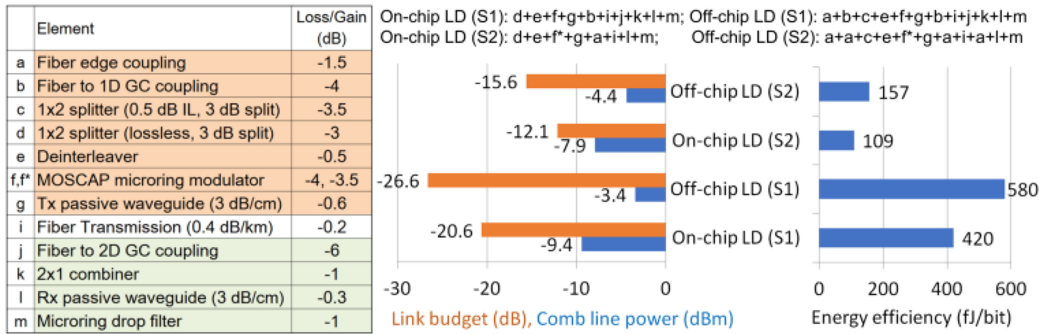

	Element	Loss/Gain (dB)
a	Fiber edge coupling	-1.5
b	Fiber to 1D GC coupling	-4
c	1x2 splitter (0.5 dB IL, 3 dB split)	-3.5
d	1x2 splitter (lossless, 3 dB split)	-3
e	Deinterleaver	-0.5
f,f*	MOSCAP microring modulator	-4, -3.5
g	Tx passive waveguide (3 dB/cm)	-0.6
i	Fiber Transmission (0.4 dB/km)	-0.2
j	Fiber to 2D GC coupling	-6
k	2x1 combiner	-1
l	Rx passive waveguide (3 dB/cm)	-0.3
m	Microring drop filter	-1

Fig. 14. Optical loss table of elements in the proposed DWDM link and calculated link budget, energy efficiency and required power for each of 20 individual comb lines.

couplers. PM fiber instead of standard SMF is used to eliminate the polarization diversity 2D GC and power combiner on the Rx side. Then appreciable link loss budget reduction is resulted as shown in Fig. 14. This design makes it possible to eliminate booster SOAs by simply adjusting minimal comb line power to −7.9 and −4.4 dBm for on- and off-chip laser configurations, respectively. Further improvement to 10% WPE for both on- and off-chip comb lasers up to 50 °C target operation temperature are reasonable, And IL and V_{pp} of the microring modulator could be reduced to −3.5 dB and 1 V respectively after design and process optimiation. As a result of passive loss shrinkage and active component elimination/improvement, respective energy efficiencies are 109 and 157 fJ/bit for on- and off-chip laser configurations. It is at least 100× better than 100 Gb/s pluggable TRx modules in the market now. Once fabrication is transferred to a foundry for lower passive waveguide loss and more than 20 wavelengths are available from comb source for larger fan-out scale, we expect another 2-4× improvement on energy efficiency. It is necessarily noted that a typical thermal tuning efficiency measured on a Si microring with similar dimension is around 0.14 nm/mW in our lab, equivalent to an energy efficiency of 393 fJ/bit to shift one channel spacing of 120 GHz (∼0.687 nm in O-band). It would be even more when tuning on deinterleavers is necessary. Therefore conventional thermal tuning can easily dominate the total link energy efficiency when it gets into the sub-pJ/bit regime. Higher data rate will lower the thermal tuning energy share but come with potentially higher energy bill and cost from the driver and DSP chips. Not only does the athermal link architecture here remove the largest aggregated power consumption contribution of a single category, but also allows closer device proximity and shorter bus waveguide, much shorter than 100 μm spacing between microrings in previous calculations, which is eventually limited by the packaging scheme.

VI. Discussion and Future Work

In addition to continuous optimization on individual passive and active components, ultimate DWDM TRx system demonstration involves potential III–V and SiGe process co-integration, wavelength tracking and coordination among laser, deinterleavers, microring modulators and drop filters in the Rx side. Typically multiple monitor PDs (MPDs) are required in a TRx system even if only broad-band components like MZI modulators are used. They provide useful information, such as laser output power, lasing wavelength with respect to optimal operation spot in modulator and drop filter window, or their resonance drift, etc. to assist control algorithm adjusting each component accordingly. The optical monitoring is normally implemented by adding directional couplers or multi-mode interferometers along the optical paths or a private bus waveguide to each microring resonator. A small fraction of the optical power is tapped off and then absorbed by MPDs. Very recently inspired by some prior work [110], we developed a hitless optical monitor particularly suitable for our MOSCAP structure [111]. It leverages the same design, fabrication and metal contacts for the MOSCAP to quantitatively measure the change in waveguide conductance owing to the free carriers generated from defects and surface state absorption of photons in Si waveguide. It harvests the free carriers existing in the Si waveguide anyway rather than adding additional optical loss, and reduces complexity in layout, fabrication and packaging drastically as well. Furthermore, the same concept was also successfully applied to a heterogeneous MOSCAP distributed feedback laser to extract characteristic information like lasing threshold, power, efficiency, mode hop and thermal rollover [42], [112], [113]. To our best knowledge, it was the first time to measure diode laser parametric performance without using an internal or external photodetector. This technique could trigger big impact on wafer-level known-good-device/die testing, early-stage diagnosis besides the operation monitoring of optical components in a PIC. The same concept is being adopted in the heterogeneous comb laser design in an on-going development run. Therefore, conventional MPDs are left out in Fig. 1 not just for illustrative simplicity but also likely unnecessity in practice in our design.

Moreover, MOSCAP-enabled athermal nearly-powerless phase tuning and hitless optical power monitoring offer more convenience in device redundancy implementation. Additional heterogeneous comb lasers, microring modulators/drop filters and MPDs cost little in term of footprint, material and fabrication. Backup MOSCAP microrings can be pre-biased at non-occupied wavelength grids, or used to suppress/monitor neighboring comb lines right outside the ones at active duty. The redundant comb laser(s) can be activated and supply new wavelength streams through a MOSCAP optical switch as soon

as the MOSCAP optical monitor inside the starting comb laser triggers a substitution signal. It will considerably relieves a major concern of many people to the system reliability of single comb laser-powered WDM PICs. Besides active components, some advanced heterogeneous GC structure (Fig. 2(g)) can be engineered on this heterogeneous platform. Similar to a demonstrated GC structure with a poly-Si overlay in [114], a properly designed III–V overlay on top of the Si could help in breaking the symmetry in light diffraction and increasing directionality towards wafer surface. Enhanced GC coupling efficiency and bandwidth are expected, which is an example of passive (not only just active) component improvement by heterogeneously integrating III–V thin film on Si.

Last but not the least, we believe that this heterogeneous platform possesses great potential for emerging applications, such as, neuromorphic computing [115], [116], Lidar [117] and bio-sensing [118]. Unique advantages of chip compactness, integrated multi-wavelength source, athermal and negligible power consumption phase control, robust operation and one-bond-for-all functionality versatility and simple fabrication will and should benefit more applications beyond optical communications.

VII. Summary

A thorough review on a DWDM TRx architecture and critical building block development were presented here. Rationale of overall benefits in term of bandwidth scalability, energy efficiency, integration density and volume manufacturability were discussed and supported by experimental demonstrations. Highlights of key component performance include more than 280 comb lines generated by a single QD laser on Si, 11.25 dB/mm on-chip gain, MOSCAP deinterleaver with over 28 dB extinction ratio, robust 28 Gb/s OOK modulation in a MOSCAP microring modulator, a record-high GBP of 585 and 32 Gb/s operation in a QD APD, and very robust low-voltage SACM SiGe APD capable of 80 Gb/s PAM4 operation with nearly 100% quantum efficiency. Several successful link demonstrations based on discrete building blocks proved the concept and further qualified components from the system performance perspective. After removing huge I/O losses to access each component, we project energy efficiency as good as $\sim$100 fJ/bit for a fully-integrated TRx on Si with 1 Tb/s aggregated bandwidth.

More and more groups share and resonate the same vision with us and are developing different versions of frequency comb-powered, microring resonator-based DWDM direct detection TRx architectures, chips [119], [120] and product [121]–[123]. Future work on fully functional TRx system integration including electronic driver integration and system-level control algorithm development brings new challenges and excitement as well. We believe that more applications beyond communications will be enabled and beneficial from this wavelength and spatial division multiplexing architecture, high-quality materials, simple and volume manufacture-friendly integration platform, dense integration, robust device operation and athermal agile phase control covered in this work.

References

[1] *World's Biggest*. [Online]. Available: http://worldstopdatacenters.com/biggest/

[2] S. Yamaoka *et al.*, "Directly modulated membrane lasers with 108 GHz bandwidth on a high-thermal- conductivity silicon carbide substrate," *Nature Photon.*, vol. 15, pp. 28–35, 2021.

[3] Y. Matsui *et al.*, "Low-chirp isolator-free 65-GHz-bandwidth directly modulated lasers," *Nature Photon.*, vol. 15, pp. 59–63, 2021.

[4] H. Zhang *et al.*, "800 Gbit/s transmission over 1 km single-mode fiber using a four-channel silicon photonic transmitter," *Photon. Res.*, vol. 8, pp. 1776–1782, 2020.

[5] M. Jacques *et al.*, "200 Gbit/s net rate transmission over 2 km with a silicon photonic segmented MZM," in *Proc. Inst. Eng. Technol.*, 2019, pp. 1–4.

[6] J. Zhang *et al.*, "Demonstration of 260-Gb/s single-lane EML-Based PS-PAM-8 IM/DD for datacenter interconnects," in *Proc. Opt. Fiber Commun. Conf.*, San Diego, CA,USA, 2019, Art. no. W4I.4.

[7] Y. Zhang *et al.*, "200 Gbit/s optical PAM4 modulation based on silicon microring modulator," in *Proc. Eur. Conf. Opt. Commun.*, 2020, pp. 1–4.

[8] R. G. Beausoleil *et al.*, "A nanophotonic interconnect for high-performance many-core computation," in *Proc. Integr. Photon. Nanophotonics Res. Appl.*, Boston, MA, USA, 2008, pp. 365–367.

[9] J. H. Ahn *et al.*, "Devices and architectures for photonic chip-scale integration," *Appl. Phys. A*, vol. 95, pp. 989–997, 2009.

[10] M. A. Seyedi, C.-H. Chen, M. Fiorentino, and R. Beausoleil, "Error-free DWDM transmission and crosstalk analysis for a silicon photonics transmitter," *Opt. Exp.*, vol. 23, pp. 32968–32976, 2015.

[11] M. Georgas, J. Leu, B. Moss, C. Sun, and V. Stojanović, "Addressing link-level design tradeoffs for integrated photonic interconnects," in *Proc. IEEE Custom Integr. Circuits Conf.*, 2011, pp. 1–8.

[12] C.-H. Chen *et al.*, "A comb laser-driven DWDM silicon photonic transmitter based on microring modulators," *Opt. Exp.*, vol. 23, pp. 21541–21548, 2015.

[13] J. Youn *et al.*, "3D-Integrated DWDM silicon photonics receiver," in *Proc. OSA Adv. Photon. Congr. 2021*, WA, DC, 2021, Art. no. ITu4A.4.

[14] D. Liang, M. Fiorentino, and R. G. Beausoleil, "VLSI photonics for next-generation datacenters and exascale computing," in *Proc. ARPA-E ENLITENED Prog. Kick-Off Meeting*, San Francisco, 2017.

[15] D. Liang *et al.*, "Fully-Integrated DWDM heterogenous DML transmitters for high-performance computing," *J. Lightw. Technol.*, vol. 38, pp. 3322–3337, 2020.

[16] D. Liang *et al.*, "Integrated green DWDM photonics for next-gen high-performance computing," in *Proc. Opt. Fiber Commun. Conf.*, San Diego, CA, USA, 2020, pp. 1–3.

[17] G. Kurczveil, A. Seyedi, D. Liang, M. Fiorentino, and R. G. Beausoleil, "Error-free operation in a hybrid-silicon quantum dot comb laser," *Photon. Technol. Lett.*, vol. 30, pp. 71–74, 2018.

[18] M. L. Davenport, S. Liu, and J. E. Bowers, "Integrated heterogeneous silicon/III–V mode-locked lasers," *Photon. Res.*, vol. 6, pp. 468–478, 2018.

[19] Z. Wang *et al.*, "A III–V-on-Si ultra-dense comb laser," *Light: Sci. Appl.*, vol. 6, 2017, Art. no. e16260.

[20] S. Liu *et al.*, "490 fs pulse generation from passively mode-locked single section quantum dot laser directly grown on on-axis GaP/Si," *Inst. Eng. Technol.*, vol. 54, pp. 432–433, 2018.

[21] A. Gubenko *et al.*, "Error-free 10 Gbit/s transmission using individual Fabry-Perot modes of low-noise quantum-dot laser," *Inst. Eng. Technol.*, vol. 43, pp. 1430–1431, 2007.

[22] G. Liu *et al.*, "InAs/InP quantum dot mode-locked laser with an aggregate 12.544 Tbit/s transmission capacity," *Opt. Exp.*, vol. 30, pp. 3205–3214, 2022.

[23] V. Cao *et al.*, "Recent progress of quantum dot lasers monolithically integrated on si platform," *Front. Phys.*, vol. 10, 2022, Art. no. 839953.

[24] G. Kurczveil, A. Descos, D. Liang, and R. G. Beausoleil, "Hybrid silicon quantum dot comb laser with record wide comb width," in *Proc. OSA Tech. Dig.*, 2020, Art. no. FTu6E.6.

[25] D. Bimberg *et al.*, "InGaAs-GaAs quantum-dot lasers," *IEEE J. Sel. Topics Quantum Electron.*, vol. 3, no. 2, pp. 196–205, Apr. 1997.

[26] G. Kurczveil, D. Liang, M. Fiorentino, and R. G. Beausoleil, "Robust hybrid quantum dot laser for integrated silicon photonics," *Opt. Exp.*, vol. 24, pp. 16167–16174, 2016.

[27] S. Liu *et al.*, "High-performance O-band quantum-dot semiconductor optical amplifiers directly grown on a CMOS compatible silicon substrate," *ACS Photon.*, vol. 6, pp. 2523–2529, 2019.

[28] M. Ashkan Seyedi *et al.*, "Crosstalk analysis of ring resonator switches for all-optical routing," *Opt. Exp.*, vol. 24, pp. 11668–11676, 2016.

[29] K. Padmaraju, X. Zhu, L. Chen, M. Lipson, and K. Bergman, "Intermodulation crosstalk characteristics of WDM silicon microring modulators," *IEEE Photon. Technol. Lett.*, vol. 26, no. 14, pp. 1478–1481, Jul. 2014.

[30] W. Bogaerts *et al.*, "Silicon microring resonators," *Laser Photon. Rev.*, vol. 6, pp. 47–73, 2012.

[31] D. Liang *et al.*, "A tunable hybrid III–V-on-Si MOS microring resonator with negligible tuning power consumption," in *Proc. Opt. Fiber Commun. Conf. Exhib.*, Anaheim, CA, USA: OSA, 2016, pp. 1–3.

[32] X. Huang *et al.*, "Heterogeneous MOS microring resonators," in *Proc. IEEE Photon. Conf.*, Orlando, FL, USA, 2017, pp. 121–122.

[33] S. Srinivasan, D. Liang, and R. G. Beausoleil, "Heterogeneous SISCAP microring modulator for high-speed optical communication," in *Proc. Eur. Conf. Opt. Commun.*, 2020, pp. 1–3.

[34] S. Srinivasan, D. Liang, and R. G. Beausoleil, "Heterogeneous III–V/Si MOSCAP micro-ring modulators," *under preparation*.

[35] S. Cheung *et al.*, "Ultra-power-efficient heterogeneous III–V/Si (De-) interleavers for DWDM optical links," *Photon. Res.*, vol. 10, pp. A22–A34, 2022.

[36] D. Liang, X. Huang, G. Kurczveil, M. Fiorentino, and R. G. Beausoleil, "Integrated finely tunable microring laser on silicon," *Nature Photon.*, vol. 10, pp. 719–722, 2016.

[37] C. Lacava *et al.*, "Design and characterization of low-loss 2D grating couplers for silicon photonics integrated circuits," in *Proc. SPIE*, vol. 9752, 2016, Art. no. 97520V.

[38] Y. Yuan *et al.*, "Avalanche photodetectors on silicon photonics," *IoP J. Semiconductors*, vol. 43, 2021, Art. no. 021301.

[39] Z. Huang *et al.*, "25 Gbps low-voltage waveguide Si-Ge avalanche photodiode," *Optica*, vol. 3, pp. 793–798, 2016.

[40] S. A. Srinivasan *et al.*, "27 GHz silicon-contacted waveguide-coupled ge/si avalanche photodiode," *J. Lightw. Technol.*, vol. 38, pp. 3044–3050, 2020.

[41] J. Zhang, B. P.-P. Kuo, and S. Radic, "64Gb/s PAM4 and 160Gb/s 16QAM modulation reception using a low-voltage Si-Ge waveguide-integrated aPD," *Opt. Exp.*, vol. 28, pp. 23266–23273, 2020.

[42] D. Liang *et al.*, "High-performance quantum-dot distributed feedback laser on silicon for high-speed modulations," *Optica*, vol. 8, pp. 591–593, 2021.

[43] Y. Wang *et al.*, "Monolithic quantum-dot distributed feedback laser array on silicon," *Optica*, vol. 5, pp. 528–533, 2018.

[44] D. Liang *et al.*, "Heterogeneous silicon light sources for datacom applications," *Opt. Fiber Technol.*, vol. 44, pp. 43–52, 2018.

[45] J. X. Chen *et al.*, "Tuning InAs/GaAs quantum dot properties under Stranski-Krastanov growth mode for 1.3 μm applications," *J. Appl. Phys.*, vol. 91, pp. 6710–6716, 2002.

[46] Y. Arakawa, T. Nakamura, and J. Kwoen, "Chapter three - Quantum dot lasers for silicon photonics," in *Semiconductors and Semimetals*, vol. 101. S. Lourdudoss, J. E. Bowers, and C. Jagadish, Eds., Amsterdam, The Netherlands; New York, NY, USA: Elsevier, 2019, pp. 91–138.

[47] J. C. Norman *et al.*, "A review of high-performance quantum dot lasers on silicon," *IEEE J. Quantum Electron.*, vol. 55, no. 2, Apr. 2019, Art no. 2000511.

[48] Y. Arakawa and H. Sakaki, "Multidimensional quantum well laser and temperature dependence of its threshold current," *Appl. Phys. Lett.*, vol. 40, pp. 939–941, 1982.

[49] M. Sugawara and M. Usami, "Handling the heat," *Nature Photon.*, vol. 3, pp. 30–31, 2009.

[50] S. Chen *et al.*, "Electrically pumped continuous-wave III–V quantum dot lasers on silicon," *Nature Photon.*, vol. 10, pp. 307–311, 2016.

[51] A. Y. Liu, S. Srinivasan, J. Norman, A. C. Gossard, and J. E. Bowers, "Quantum dot lasers for silicon photonics [Invited]," *Photon. Res.*, vol. 3, pp. B1–B9, 2015.

[52] C. Meuer *et al.*, "Static gain saturation in quantum dot semiconductor optical amplifiers," *Opt. Exp.*, vol. 16, pp. 8269–8279, 2008.

[53] S. Srinivasan *et al.*, "8×25 Gb/s DWDM transmitter link demonstration on a heterogeneous silicon photonic platform," in *Proc. Integr. Photon. Res., Silicon Nanophotonics*, 2021, Art. no. ITu3A.4.

[54] S. Liu *et al.*, "High-channel-count 20 GHz passively mode-locked quantum dot laser directly grown on Si with 4.1 Tbit/s transmission capacity," *Optica*, vol. 6, pp. 128–134, 2019.

[55] G. Kurczveil *et al.*, "On-chip hybrid silicon quantum dot comb laser with 14 error-free channels," in *Proc. ISLC*, Santa Fe, NM, USA, 2018, pp. 1–2.

[56] B. Dong *et al.*, "Frequency comb dynamics of a 1.3 μm hybrid-silicon quantum dot semiconductor laser with optical injection," *Opt. Lett.*, vol. 44, pp. 5755–5758, 2019.

[57] G. Kurczveil *et al.*, "High-temperature error-free operation in a heterogeneous silicon quantum dot comb laser," in *Proc. Opt. Fiber Commun. Conf.*, San Diego, CA, USA, 2022, pp. 1–3.

[58] A. Descos, G. Kurczveil, D. Liang, and R. Beausoleil, "Heterogeneous O-Band InAs/GaAs quantum-dot optical amplifier on silicon," in *Proc. Asia Commun. Photon. Conf.*, Shanghai, China, 2021, pp. 1–3.

[59] D. Bimberg *et al.*, "Influence of P-doping in quantum dot semiconductor optical amplifiers at 1.3 μm," in *Proc. 11th Int. Conf. Transparent Opt. Netw.*, 2009, pp. 1–4.

[60] Z. Bakonyi *et al.*, "High-gain quantum-dot semiconductor optical amplifier for 1300 nm," *IEEE J. Quantum Electron.*, vol. 39, no. 11, pp. 1409–1414, Nov. 2003.

[61] H. Wang *et al.*, "Temperature independent optical amplification in uncooled quantum dot optical amplifiers," in *Proc. Conf. Opt. Fiber Commun./Nat. Fiber Optic Engineers Conf.*, 2008, pp. 1–3.

[62] N. K. Dutta and A. W. Qiang, *Semiconductor Optical Amplifiers*. Singapore: World Scientific Publishing Company, 2013.

[63] H. Liu *et al.*, "Long-wavelength InAs/GaAs quantum-dot laser diode monolithically grown on Ge substrate," *Nature Photon.*, vol. 5, pp. 416–419, 2011.

[64] J. Kwoen *et al.*, "All MBE grown InAs/GaAs quantum dot lasers on on-axis Si (001)," *Opt. Exp.*, vol. 26, pp. 11568–11576, 2018.

[65] S. Liu and A. Khope, "Latest advances in high-performance light sources and optical amplifiers on silicon," *J. Semiconductors*, vol. 42, 2021, Art. no. 041307.

[66] Y. Wan, J. Norman, S. Liu, A. Liu, and J. E. Bowers, "Quantum dot lasers and amplifiers on silicon: Recent advances and future developments," *IEEE Nanotechnol. Mag.*, vol. 15, no. 2, pp. 8–22, Apr. 2021.

[67] J. Norman *et al.*, "Epitaxial integration of high-performance quantum-dot lasers on silicon," in *Proc. SPIE*, 2020, vol. 11285, Art. no. 1128504.

[68] D. Jung *et al.*, "Recent advances in inas quantum dot lasers grown on on-axis (001) silicon by molecular beam epitaxy," *Physica Status Solidi (a)*, vol. 216, 2019, Art. no. 1800602.

[69] T. Hiraki *et al.*, "Heterogeneously integrated III–V/Si MOS capacitor Mach–Zehnder modulator," *Nature Photon.*, vol. 11, pp. 482–485, 2017.

[70] J.-H. Han *et al.*, "Efficient low-loss InGaAsP/Si hybrid MOS optical modulator," *Nature Photon.*, vol. 11, pp. 486–490, 2017.

[71] T. Thiessen *et al.*, "30 GHz heterogeneously integrated capacitive InP-on-Si Mach–Zehnder modulators," *Opt. Exp.*, vol. 27, pp. 102–109, 2019.

[72] M. Webster *et al.*, "An efficient MOS-capacitor based silicon modulator and CMOS drivers for optical transmitters," in *Proc. Int. Conf. Group IV Photon.*, 2014, pp. 1–2.

[73] A. W. Fang *et al.*, "Electrically pumped hybrid AlGaInAs-silicon evanescent laser," *Opt. Exp.*, vol. 14, pp. 9203–9210, 2006.

[74] R. Soref and B. Bennett, "Electrooptical effects in silicon," *IEEE J. Quantum Electron.*, vol. 23, no. 1, pp. 123–129, Jan. 1987.

[75] P. Dong *et al.*, "Thermally tunable silicon racetrack resonators with ultralow tuning power," *Opt. Exp.*, vol. 18, pp. 20298–20304, 2010.

[76] R. Wu *et al.*, "Compact models for carrier-injection silicon microring modulators," *Opt. Exp.*, vol. 23, pp. 15545–15554, 2015.

[77] S. Cheung *et al.*, "Ultra-power efficient heterogeneous III–V/Si de-interleavers for DWDM optical links," in *Proc. IEEE 17th Int. Conf. Group IV Photon.*, 2021, pp. 1–2.

[78] L.-W. Luo *et al.*, "High bandwidth on-chip silicon photonic interleaver," *Opt. Exp.*, vol. 18, pp. 23079–23087, 2010.

[79] N. Zhou *et al.*, "Reconfigurable and tunable compact comb filter and (de)interleaver on silicon platform," *Opt. Exp.*, vol. 26, pp. 4358–4369, 2018.

[80] Q. Sun, L. Zhou, L. Lu, G. Zhou, and J. Chen, "Reconfigurable high-resolution microwave photonic filter based on dual-ring-assisted MZIs on the Si_3N_4 platform," *IEEE Photon. J.*, vol. 10, no. 6, pp. 1–12, Dec. 2018.

[81] A. Rizzo, Q. Cheng, S. Daudlin, and K. Bergman, "Ultra-broadband interleaver for extreme wavelength scaling in silicon photonic links," *IEEE Photon. Technol. Lett.*, vol. 33, no. 1, pp. 55–58, Jan. 2021.

[82] C. K. Madsen and J. H. Zhao, *Optical Filter Design and Analysis: A Signal Processing Approach*. New York, NY, USA: Wiley, 1999.

[83] A. Liu *et al.*, "A high-speed silicon optical modulator based on a metal-oxide-semiconductor capacitor," *Nature*, vol. 427, pp. 615–618, 2004.

[84] M. de Cea, A. H. Atabaki, and R. J. Ram, "Power handling of silicon microring modulators," *Opt. Exp.*, vol. 27, pp. 24274–24285, 2019.

[85] G. Roelkens *et al.*, “Integration of InP/InGaAsP photodetectors onto silicon-on-insulator waveguide circuits,” *Opt. Exp.*, vol. 13, pp. 10102–10108, 2005.
[86] H. Park *et al.*, “A hybrid algainas-silicon evanescent waveguide photodetector,” *Opt. Exp.*, vol. 15, pp. 6044–6052, 2007.
[87] L. Shen *et al.*, “High-bandwidth uni-traveling carrier waveguide photodetector on an InP-membrane-on-silicon platform,” *Opt. Exp.*, vol. 24, pp. 8290–8301, 2016.
[88] G. Kurczveil, D. Liang, M. Fiorentino, and R. G. Beausoleil, “A compact, high-speed, highly efficient hybrid silicon photodetector,” in *Proc. IEEE Opt. Interconnects Conf.*, San Diego, CA, USA, 2016, pp. 8–9.
[89] B. Tossoun *et al.*, “32 Gbps heterogeneously integrated quantum dot waveguide avalanche photodiodes on silicon,” *Opt. Lett.*, vol. 46, pp. 3821–3824, 2021.
[90] B. Tossoun *et al.*, “InAs quantum dot waveguide photodiodes heterogeneously integrated on silicon,” *Optica*, vol. 6, pp. 1277–1281, 2019.
[91] B. Chen *et al.*, “Low dark current high gain inas quantum dot avalanche photodiodes monolithically grown on Si,” *ACS Photon.*, vol. 7, pp. 528–533, 2020.
[92] B. Kochman, “Electronic phenomena in Self-organized quantum dots: Theory and applications,” Ph.D. dissertation, Dept. Elect. Comput. Eng., Univ. Michigan, Ann Arbor, USA, 2002.
[93] Y.-J. Ma *et al.*, “Enhanced carrier multiplication in inas quantum dots for bulk avalanche photodetector applications,” *Adv. Opt. Mater.*, vol. 5, 2017, Art. no. 1601023.
[94] I. Sandall *et al.*, “1300 nm Wavelength InAs quantum dot photodetector grown on silicon,” *Opt. Exp.*, vol. 20, pp. 10446–10452, 2012.
[95] T. Umezawa *et al.*, “Polarization dependence of avalanche multiplication factor in 1.5 μm quantum dot waveguide photodetector,” in *Proc. Conf. Lasers Electro Opt.*, San Jose, CA, 2016, Art. no. SM4E.8.
[96] W. Sun *et al.*, “High-gain InAs avalanche photodiodes,” *IEEE J. Quantum Electron.*, vol. 49, no. 2, pp. 154–161, Feb. 2013.
[97] Y. Yuan *et al.*, “High-Speed Si/Ge avalanche photodiodes with enhanced responsivity,” in *Proc. Integr. Photon. Res., Silicon Nanophotonics*, 2021, Art. no. IM5A.1.
[98] Y. Yuan *et al.*, “High responsivity Si-Ge waveguide avalanche photodiodes enhanced by loop reflector,” *IEEE J. Sel. Topics Quantum Electron.*, vol. 28, no. 2, Mar./Apr. 2022, Art. no. 3800508.
[99] Y. Kang *et al.*, “Monolithic germanium/silicon avalanche photodiodes with 340 GHz gain–bandwidth product,” *Nature Photon.*, vol. 3, pp. 59–63, 2009.
[100] X. Zeng *et al.*, “Silicon-germanium avalanche photodiodes with direct control of electric field in charge multiplication region,” *Optica*, vol. 6, pp. 772–777, 2019.
[101] J. Verbist *et al.*, “40-Gb/s PAM-4 transmission over a 40 km amplifier-less link using a Sub-5V Ge APD,” *IEEE Photon. Technol. Lett.*, vol. 29, no. 24, pp. 2238–2241, Dec. 2017.
[102] L. Virot *et al.*, “Germanium avalanche receiver for low power interconnects,” *Nature Commun.*, vol. 5, pp. 4957, 2014.
[103] B. Wang *et al.*, “64 Gb/s low-voltage waveguide SiGe avalanche photodiodes with distributed Bragg reflectors,” *Photon. Res.*, vol. 8, pp. 1118–1123 2020.
[104] Y. Yuan *et al.*, “64 Gbps PAM4 Si-Ge waveguide avalanche photodiodes with excellent temperature stability,” *J. Lightw. Technol.*, vol. 38, pp. 4857–4866, 2020.
[105] J. Shi, Y. Wu, Z. Li, and P. Chen, “Impact-ionization-induced bandwidth-enhancement of a Si–SiGe-Based avalanche photodiode operating at a wavelength of 830 nm with a gain-bandwidth product of 428 GHz,” *IEEE Photon. Technol. Lett.*, vol. 19, no. 7, pp. 474–476, Apr. 2007.
[106] W. S. Zaoui *et al.*, “Frequency response and bandwidth enhancement in Ge/Si avalanche photodiodes with over 840GHz gain-bandwidth-product,” *Opt. Exp.*, vol. 17, pp. 12641–12649, 2009.
[107] L. Chang, S. Liu, and J. E. Bowers, “Integrated optical frequency comb technologies,” *Nature Photon.*, vol. 16, pp. 95–108, 2022.
[108] S. Srinivasan *et al.*, “160Gb/s optical link using Quantum-Dot comb laser source and SiGe APD,” in *Proc. IEEE Photon. Conf.*, 2020, pp. 1–2.
[109] S. Mathai *et al.*, “Detachable 1x8 single mode optical interface for DWDM microring silicon photonic transceivers,” in *Proc. SPIE*, 2020, vol. 11286, Art. no. 112860A.
[110] S. Grillanda *et al.*, “Non-invasive monitoring and control in silicon photonics using CMOS integrated electronics,” *Optica*, vol. 1, pp. 129–136, 2014.
[111] S. Srinivasan, D. Liang, and R. G. Beausoleil, “Non-invasive light monitoring for heterogeneous photonic integrated circuits,” in *Proc. IEEE Photon. Conf.*, 2021, pp. 1–2.
[112] S. Srinivasan, D. Liang, and R. G. Beausoleil, “*In-situ* light measurement in heterogeneous gain media,” in *Proc. 27th Int. Semicond. Laser Conf.*, Germany, 2021, pp. 1–2.
[113] D. Liang *et al.*, “A heterogeneous O-band quantum-dot DFB laser with integrated MOS capacitive control,” in *Proc. IEEE Photon. Conf.*, 2020, pp. 1–2.
[114] G. Roelkens, D. Van Thourhout, and R. Baets, “High efficiency Silicon-on-Insulator grating coupler based on a poly-Silicon overlay,” *Opt. Exp.*, vol. 14, pp. 11622–11630, 2006.
[115] X. Xiao *et al.*, “Large-scale and energy-efficient tensorized photonic neural networks on III–V-on-Silicon MOSCAP platform,” *APL Photon.*, vol. 6, pp. 126107 2022, 2021.
[116] B. Tossoun, X. Sheng, J. P. Strachan, and D. Liang, “The memristor laser,” in *Proc. IEEE Int. Electron Devices Meeting*, 2020, pp. 7.6.1–7.6.4.
[117] C. Benko, E. Kadlec, Z. Barber, and R. Reibel, “FMCW lidar for autonomous vehicles,” in *Proc. SPIE*, 2021, vol. 11668, Art. no. 116680N.
[118] Rockley Photonics unveils end-to-end digital health monitoring solution based on spectrophotometer-on-a-chip sensing module, 2021. [Online]. Available: https://rockleyphotonics.com/rockley-unveils-end-to-end-digital-health-monitoring-solution/
[119] A. Malik *et al.*, “Low power consumption silicon photonics datacenter interconnects enabled by a parallel architecture,” in *Proc. Opt. Fiber Commun. Conf.*, WA, DC, 2021, Art. no. W6A.3.
[120] A. Rizzo *et al.*, “Kerr comb-driven silicon photonic transmitter,” in *Proc. Opt. Fiber Commun. Conf.*, WA, DC, 2021, Art. no. Th4A.5.
[121] M. W. Media. Ranovus Announces Second-Generation "Co-Packaged Optics" Chip for Hyperscale Data Center Applications, 2021. [Online]. Available: https://ranovus.com/ranovus-announces-second-generation-co-packaged-optics-chip-for-hyperscale-data-center-applications/
[122] Z. G. Lu *et al.*, “An InAs/InP quantum dot C-band coherent comb laser,” in *Proc. Opt. Fiber Commun. Conf.*, San Diego, CA, 2018, Art. no. Th1I.4.
[123] Z. Lu, “Quantum-dot coherent comb lasers for terabit optical networking systems,” in *Proc. SPIE*, 2019, vol. 10921, Art. no. 109210N.

Di Liang (Senior Member, IEEE) received the B.S. degree in optical engineering from Zhejiang University, Hangzhou, China, and the M.S. and Ph.D. degrees in electrical engineering from the University of Notre Dame, Notre Dame, IN, USA. He is currently a Distinguished Technologist with Hewlett Packard Labs. He has authored or coauthored one book, seven book chapters, and more than 250 journal and conference papers. His research interests include silicon and III–V photonics, diode lasers, high-speed optical monitors and photodiodes, heterogeneous integration techniques and micro/nanophotonics fabrication. He is a Fellow of Optica Society.

Sudharsanan Srinivasan (Member, IEEE) received the bachelor’s degree in engineering physics from the Indian Institute of Technology Madras, Chennai, India, and the master’s and Ph.D. degrees from the University of California, Santa Barbara, CA, USA. He is currently a Research Scientist with Hewlett Packard Enterprise. He has authored or coauthored more than 30 journal papers and two book chapters. His research interests include integrated diode lasers, modulators and photodetectors, electronic photonic co-integration, heterogeneous material integration, and nanofabrication technology.

Geza Kurczveil (Member, IEEE) received the Ph.D. degree in electrical and computer engineering from the University of California, Santa Barbara, CA, USA, in 2012. He is currently a Research Scientist with HPE’s Large-Scale Integrated Photonics Lab, Santa Barbara, CA, USA. He is also working on optical buffers. He has authored or coauthored more than 50 journal and conference papers. His current research interests include comb lasers, silicon photonic integrated circuits, and nano-photonics.

Bassem Tossoun received the B.S. degree in computer engineering and the M.S. degree in electrical engineering from Cal Poly San Luis Obispo, San Luis Obispo, CA, USA, in 2014, and the Ph.D. degree in electrical engineering from the the University of Virginia, Charlottesville, VA, USA, in 2019. He is currently a Research Scientist with Hewlett Packard Labs, working on quantum dot photodiodes and memristor photonics for next-generation supercomputers. His research interests include silicon photonics and the design, fabrication, and characterization of optoelectronic devices.

Stanley Cheung (Member,IEEE) received the B.S. degree in electrical engineering from the University of Southern California, Los Angeles, CA, USA, the M.S. degree in electrical engineering from Columbia University, New York, NY, USA, and the Ph.D. degree in electrical engineering from the University of California, Davis, CA, USA. He is currently a Senior Research Scientist with Hewlett-Packard Laboratories, Milpitas, CA, USA, and is engaged in large-scale integrated photonics. His research interests include heterogeneous III–V/Si lasers/SOAs, mode-locked semiconductor lasers, widely tunable lasers, and silicon photonic integrated circuits.

Yuan Yuan received the B.S. degree in electrical engineering from the Nanjing University of Aeronautics and Astronautics, Nanjing, China, in 2016, and the Ph.D. degree in electrical engineering from the University of Virginia, Charlottesville, VA, USA, in 2019. He is currently a Research Scientist with Hewlett Packard Labs of Hewlett Packard Enterprise. His research interests include avalanche photodiodes, single photon counting, and III–V and silicon photonics. He is a Member of OSA.

Antoine Descos received the graduation degree from the French Engineer School, Ecole Centrale de Lyon, Écully, France, in 2010, majored in micro-technology, and the master's degree in micro-technology from University Claude Bernard Lyon 1, Villeurbanne, France, in 2010, and the Ph.D. degree in physics from Ecole Centrale de Lyon, France, in 2014. He is currently a Research Engineer with the Large Scale Integrated Photonics in the Systems Research Laboratory, Hewlett Packard Labs. He is also working with the CEA-LETI, Grenoble, France. His research focuses on the hybrid III–V on silicon lasers technology. He has designed, fabricated, and characterized different laser kind mainly for telecommunication purpose. He participated in 40 papers and conference proceedings.

Yingtao Hu received the B.S. degree in material science from Central South University, Changsha, China, in 2007, and the Ph.D. degree in physical electronics from the Institute of Semiconductors, Chinese Academy of Sciences, Beijing, China, in 2012. From 2012 to 2015, he was a Postdoctoral Researcher with IMEC and the University of Ghent, Ghent, Belgium, where he worked on graphene modulators on silicon. He is currently a Research Scientist with Hewlett Packard Labs, California, USA. His research focuses on hybrid IIIV-on-Si photonic devices and integration.

Zhihong Huang received the B.S. degree in physics from Peking University, Beijing, China, and the M.S. and Ph.D. degrees in electrical engineering from the University of Texas at Austin, Austin, TX, USA. She is currently a Principal Research Scientist with Hewlett Packard Labs, leading the development of low power optical transceivers for optical interconnects. She has authored or coauthored more than 80 journal and conference papers, and was granted by two dozen U.S./international patents with another dozen pending. Her research interests include silicon photonics, optical transceivers, single photon avalanche photodiodes, and also quantum information processing using diamond defect centers.

Peng Sun (Member, IEEE) received the Ph.D. degree in electrical engineering from The Ohio State University, Columbus, OH, USA, in 2012. From 2018 to 2021, he was a Senior Engineer with Luxtera Inc., Calrsbad, CA, USA from 2012 to 2018, and a Research Engineer with Hewlett Packard Labs. He is currently with Nvidia.

Thomas Van Vaerenbergh received the master's degree in applied physics and the Ph.D. degree in photonics from Ghent University, Ghent, Belgium, in 2010 and 2014, respectively. Since 2014, he has been with Hewlett Packard Labs, part of Hewlett Packard Enterprise. His main research interests include optical computing, accelerators for combinatorial optimization, and the modeling and design of passive silicon photonic devices, such as microring resonators and grating couplers.

Chong Zhang received the B.S. degree in electrical science and technology from the Harbin Institute of Technology, Harbin, China, in 2007, the M.S. degree in optical engineering from Zhejiang University, Hangzhou, China, in 2010, and the Ph.D. degree from the University of California, Santa Barbara, CA, USA, in 2016. From July 2016 to September 2018, he was with Hewlett Packard Labs, Palo Alto, CA, USA, where his research was focused on high performance heterogeneous silicon platform. His current research interests include Si and III–V photonic integrations.

Xiaoge Zeng received the B.S. degree in physics from the University of Science and Technology of China, Hefei, China, in 2008, and the Ph.D. degree in physics from the University of Colorado Boulder, Boulder, CO, USA, in 2015. Since 2016, he has been a Research Scientist with Hewlett Packard Labs, Milpitas, CA, USA. His research interests include silicon photonics, integrated optics, optical communications, nonlinear optics, and quantum optics.

Songtao Liu received the Ph.D. degree in microelectronics and solid-state electronics from the University of Chinese Academy of Sciences, Beijing, China, 2017. His research interests include III–V/silicon photonic integrated circuits, semiconductor lasers, semiconductor physics, optical interconnects, and microwave photonics. He is currently with Intel Labs, Santa Clara, CA, USA.

John E. Bowers (Life Fellow, IEEE) received the M.S. and Ph.D. degrees from Stanford University, Stanford, CA, USA. He is currently the Fred Kavli Chair in nanotechnology, and the Director of the Institute for Energy Efficiency and a Distinguished Professor with the Departments of Electrical and Computer Engineering and Materials, University of California (UC), Santa Barbara, Santa Barbara, CA, USA. He was with AT&T Bell Laboratories and Honeywell, before joining UC Santa Barbara. He is a co-founder of Nexus Photonics, Quintessent, Aurrion, Aerius Photonics, Terabit Technology and Calient Networks. Dr. Bowers is a Member of the National Academy of Engineering, National Academy of Inventors, and is a Fellow of the OSA and American Physical Society. He was the recipient of the IEEE Photonics Award, OSA/IEEE Tyndall Award, OSA Holonyak Award, IEEE LEOS William Streifer Award and the South Coast Business and Technology Pioneer and Entrepreneur of the Year awards. He and co-workers was the recipient of the EE Times Annual Creativity in Electronics Award for Most Promising Technology for the hybrid silicon laser in 2007.

Marco Fiorentino received the Ph.D. degree in physics from the University of Naples, Naples, Italy, in 2000. His doctoral work was focused on quantum optics. He is currently a Research Scientist with the System Research Laboratory, Hewlett Packard Labs, Palo Alto, CA, USA. Before working with Hewlett Packard Labs in 2005, he was with Northwestern University, Evanston, IL, USA, the University of Rome, Rome, Italy, and Massachusetts Institute of Technology, Cambridge, MA, USA. In the past, he was working on optics, high-precision measurements, and optical communications. He has authored or coauthored more than 60 papers in peer-reviewed journals and given numerous contributed and invited talks to international conferences. He is a Senior Member of the Optica Society.

Raymond G. Beausoleil (Senior Member, IEEE) received the B.S. degree in physics from Caltech, Pasadena, CA, USA, in 1980, and the Ph.D. degree in physics from Stanford University, Stanford, CA, USA, in 1986. He is currently a Senior Fellow and Senior Vice-President with Hewlett Packard Enterprise, San Jose, CA, USA, where he is the Director of the Large-Scale Integrated Photonics Lab, Hewlett Packard Labs. Prior to HPE, his research was focused on high-power all-solid-state laser and nonlinear optical systems, and numerical algorithms for computer firmware (leading to the navigation algorithms for the optical mouse). At Hewlett Packard Labs, he performs basic and applied research in microscale and nanoscale classical and quantum optics for information processing technologies. He is also an Adjunct Professor of applied physics with Stanford University, Stanford, CA, USA. He is a Fellow of the American Physical Society and the Optical Society of America. He was the recipient of the 2016 APS Distinguished Lectureship on the Applications of Physics. He has contributed to more than 600 papers and conference proceedings (including many invited papers and plenary/keynote addresses) and five book chapters. He has more than 150 patents issued, and more than four dozen pending.